



# OPTICA QUANTUM

## Anomalous Purcell decay of strongly driven inhomogeneous emitters coupled to a cavity

MICHAEL T. SOLOMON,<sup>1,2,3</sup> ID MARTIN KOPPENHÖFER,<sup>1</sup> ID MIKHAIL MAMAEV,<sup>1</sup> ID CHENG JI,<sup>1,2</sup> ID GREGORY GRANT,<sup>1,2</sup> ID IGNAS MASILIONIS,<sup>1,2</sup> ID SEAN E. SULLIVAN,<sup>2,3,4</sup> ID F. JOSEPH HEREMANS,<sup>1,2,3</sup> ID SUPRATIK GUHA,<sup>1,2,3</sup> DAVID D. AWSCHALOM,<sup>1,2,3,5</sup> ID AASHISH A. CLERK,<sup>1,2</sup> AND ALAN M. DIBOS<sup>3,6,\*</sup> ID

<sup>1</sup>Pritzker School of Molecular Engineering, University of Chicago, Chicago, Illinois 60637, USA

<sup>2</sup>Materials Science Division, Argonne National Laboratory, Lemont, Illinois 60439, USA

<sup>3</sup>Center for Molecular Engineering, Argonne National Laboratory, Lemont, Illinois 60439, USA

<sup>4</sup>Current Address: memQ Inc., Chicago, Illinois 60615, USA

<sup>5</sup>Department of Physics, University of Chicago, Chicago, Illinois 60637, USA

<sup>6</sup>Q-NEXT, Argonne National Laboratory, Lemont, Illinois 60439, USA

\*adibos@anl.gov

Received 9 February 2024; revised 4 April 2024; accepted 7 April 2024; published 18 June 2024

We perform resonant fluorescence lifetime measurements on a nanocavity-coupled erbium ensemble as a function of cavity-laser detuning and pump power. Our measurements reveal an anomalous three-fold suppression of the ensemble Purcell factor at zero cavity detuning and high pump fluence. We capture qualitative aspects of this decay rate suppression using a Tavis–Cummings model of non-interacting spins coupled to a common cavity.

© 2024 Optica Publishing Group under the terms of the [Optica Open Access Publishing Agreement](#)

<https://doi.org/10.1364/OPTICAQ.520843>

### 1. INTRODUCTION

Tailoring the interaction between atoms and their electromagnetic environment is of both fundamental interest and practical relevance, e.g., for applications in quantum communication and quantum information processing [1,2]. By tuning the photon density of states, one can drastically modify the emission properties of atoms [3], a phenomenon that underpins the thriving research area of cavity quantum electrodynamics (cQED) [4]. Prototypical cases are the interaction between a single two-level system (which we will interchangeably refer to as a “spin”) and a single mode of a radiation field [5], the collective interaction of atoms with their electromagnetic environment leading to the effects of super- and subradiance [6–8], as well as photon-mediated collective interactions [9], and large ensembles of weakly excited spins with identical or inhomogeneously broadened transition frequencies [5,10]. The limit where the spins are only weakly perturbed away from their ground or excited states is appealing, since the spin dynamics become linear and analytical studies of the dynamics become possible [11–13]. Much less is known, however, in the case of highly excited spins where the intrinsic nonlinearity of the spin dynamics due to their finite-dimensional Hilbert space needs to be taken into account.

Trapped atomic systems are the prototypical spins for investigating optical relaxation dynamics because of their coherence and homogeneity in ensembles. In cQED, there is particular interest in modifying the atom–photon coupling strength through

the use of high-quality-factor (Q) and small-mode-volume optical cavities. While significant progress has been made in integrating conventional trapped atomic systems with these types of resonators [14–16], it still remains an outstanding technical challenge to experimentally achieve high coupling with modest ensembles of atoms to probe the rich phenomena available from collective effects [17–20]. In contrast, rare-earth ions embedded in solid-state hosts and integrated with nanoscale optical cavities—which are being explored for use in quantum memories [21–24] and microwave-to-optical transduction [25,26]—have naturally long optical lifetimes that are ideally suited for optical-decay-modification experiments. These features of nanocavity-coupled rare-earth ions are typically at the expense of large inhomogeneous broadening, but this trait has recently been shown to be an important factor in the observation of collectively induced transparency [27], where the dynamics of a strongly driven and disordered ensemble can modify the steady-state system response due to an interplay of quantum interference and collective effects. Similarly in this work, we study an ensemble of rare-earth ions coupled to a relatively high-Q, small mode volume optical cavity and subjected to a resonant laser driving field. The large inhomogeneous linewidth of the ensemble and the relatively narrow resonance of the cavity enable us to explore surprising effects that manifest themselves in the dependence of the highly excited spin ensemble’s optical relaxation rate on both cavity-laser detuning and optical drive power. These occur in a regime where disorder plays a non-trivial role.

Our specific spin-cavity system consists of trivalent erbium ions ( $\text{Er}^{3+}$  or Er for brevity) incorporated into a thin layer of  $\text{TiO}_2$  grown atop silicon-on-insulator (SOI) wafers [28,29]. The Er ions are evanescently coupled to a one-dimensional (1D) photonic crystal cavity that is patterned through both the  $\text{TiO}_2$  and Si device layers. In a prior study, we attempted to measure the Purcell enhancement in Er-doped  $\text{TiO}_2$  films coupled to a nanophotonic cavity as we tuned the cavity resonance across a particular optical transition [28]. During the course of those experiments, we noticed features resembling the saturation of the Purcell enhancement at high laser pump powers. However, the overall photon collection efficiency and fluorescence signal were too low to perform sufficient sweeps of the optical drive. Here, the Er concentration is three-fold increased by growing more highly doped films and the device-to-fiber coupling efficiency is five-fold increased by incorporating an inverse taper in-coupling structure. We report anomalously slow relaxation rates in the temporal response of highly excited and inhomogeneously broadened spin ensembles. We reproduce qualitative features of this decay via semiclassical simulations with a Tavis–Cummings model of non-interacting spins coupled to a common cavity. Finally, we derive a simple toy model that provides physical intuition for this phenomenon.

## 2. EXPERIMENTAL DETAILS AND RESULTS

### 2.1. Samples and Device Fabrication

For this study, we use molecular beam deposited Er-doped  $\text{TiO}_2$  films that contain both rutile and anatase crystalline grains, as was seen in prior work [28]. Previous experiments have shown that the inclusion of undoped spacer layers surrounding a doped region can reduce optical inhomogeneous broadening for epitaxial Er:Y<sub>2</sub>O<sub>3</sub> [30] and Er: $\text{TiO}_2$  thin films [31], as well as spectral diffusion and inhomogeneous linewidth broadening for Er in polycrystalline  $\text{TiO}_2$  films [32]. However, a thick  $\text{TiO}_2$  layer is more difficult to etch anisotropically into high-Q cavities. With both of these considerations in mind, we employ a “10/10/10” heterostructure: a 10-nm undoped  $\text{TiO}_2$  buffer layer at the Si interface, a 10-nm Er-doped  $\text{TiO}_2$  layer in the middle, and a 10-nm undoped  $\text{TiO}_2$  capping layer on top. The sample is grown on a standard SOI wafer used for silicon photonics. During the molecular beam deposition of Er: $\text{TiO}_2$ , we use a substrate temperature of 390°C and metallic Er cell temperature of 900°C.

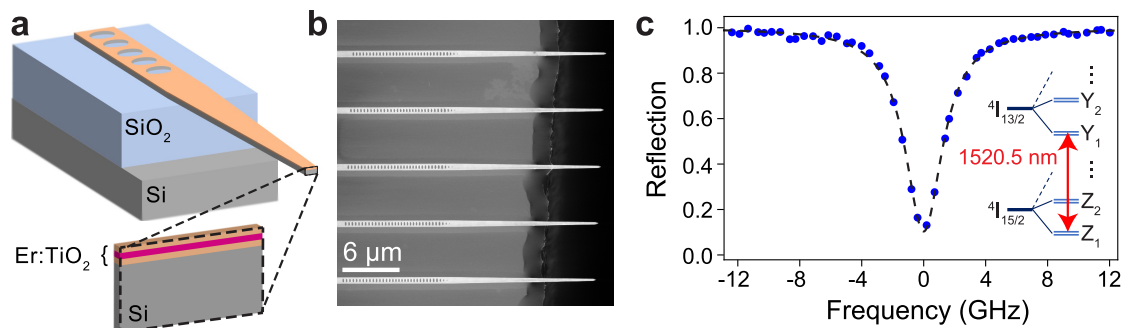


**Fig. 1.** Er-doped  $\text{TiO}_2$ -Si 1D photonic crystal cavities. (a) Schematic of fabricated devices showing the inverse taper of the waveguide extending off the chip. The inset at the end facet highlights the doped  $\text{TiO}_2$  heterostructure deposited on top of the Si device layer consisting of 10 nm of undoped  $\text{TiO}_2$ , 10 nm of doped  $\text{TiO}_2$  (~120 ppm Er, colored red), and 10 nm of undoped  $\text{TiO}_2$ . (b) Scanning electron microscope image of the nanophotonic cavity composed of elliptically shaped holes etched through the  $\text{TiO}_2$ -Si device layers and the waveguide inverse taper protruding from the chip edge. (c) Normalized laser reflection spectrum of the cavity tuned onto resonance with the  $Z_1 \rightarrow Y_1$  optical transition for Er in rutile phase  $\text{TiO}_2$  ( $\lambda = 1520.52$  nm, see inset) at a temperature of 3.5 K. Using a Lorentzian fit (dashed line), the cavity quality factor gives  $Q = (6.71 \pm 0.11) \times 10^4$ .

This Er temperature corresponds to flux that will yield ~120 (130) ppm Er if the crystal phase of the  $\text{TiO}_2$  is rutile (anatase) due to the difference in density. This corresponds to an Er-Er spacing of approximately 4.4 nm.

Our Er: $\text{TiO}_2$ -Si photonic crystal cavities are optically addressed in a one-sided configuration via a lensed optical fiber. The waveguide width and photonic crystal cavity design parameters are identical to those shown previously [28]. However, for this work, we wanted to improve the coupling efficiency between the lensed fiber and the cavity, as previous devices involved end-fiber coupling into a cleaved waveguide with an efficiency of 10–15%. To do so, we used Lumerical 3D finite-difference time-domain (FDTD) simulations to optimize the design of an inverse taper that extends off the edge of the chip, Fig. 1(a), for better mode matching to the lensed fiber [33,34], and simulation details are provided as supplementary materials (SM) in **Supplement 1**. The simulations show that an adiabatic reduction in waveguide width from 650 nm (where the cavity holes end) down to 200 nm over a 14  $\mu\text{m}$  length, allows for a fiber coupling efficiency up to 80%.

We fabricate these Er: $\text{TiO}_2$  on Si 1D photonic crystal cavities as outlined previously [28], but with additional steps to selectively undercut the inverse tapers without damaging the Si and  $\text{TiO}_2$  (complete fabrication flow is provided in **Supplement 1**, Fig. S2a). We deposit a device protection layer of conformal thermal atomic layer deposition (ALD) alumina, which covers the top surface of the sample as well as the exposed sidewalls and end facet of the inverse taper. We then cleave the SOI chip adjacent to the termini of the tapers via a precision cleaver under an optical microscope. After this, we perform an isotropic etch of the Si handle layer via  $\text{XeF}_2$ , followed by vapor HF (VHF) etching to undercut the buried  $\text{SiO}_2$ . After sufficient VHF exposure to fully remove the 2- $\mu\text{m}$  buried oxide layer underneath the suspended portion of the taper, we strip the protective alumina layer using a wet etchant and anneal the sample. SEM and optical images of the final devices are shown in Figs. 1(b) and S2b (see **Supplement 1**), respectively. It should be noted that as long as the vapor processes yield a lateral undercut length of at least 4  $\mu\text{m}$  of the 14- $\mu\text{m}$  taper, the mode is sufficiently waveguided such that minimal light is lost into the substrate (Fig. S1a, **Supplement 1**).

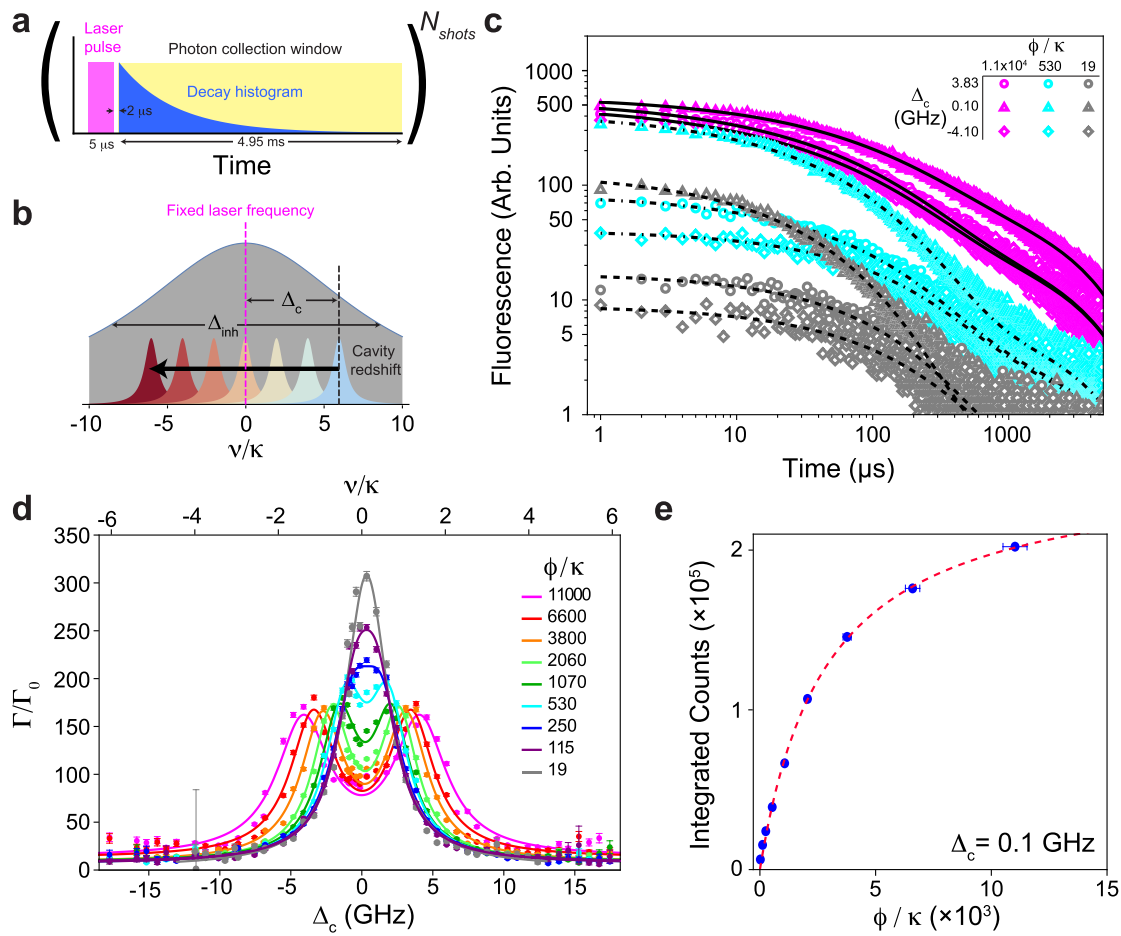


**Fig. 2.** PLE Measurements on cavity-coupled Er ensembles at 3.5 K. (a) Schematic of our photoluminescence excitation measurement sequence. We first generate a 5- $\mu$ s-long laser excitation pulse (magenta). After a 2- $\mu$ s wait time, we open an additional modulator in the collection path to start the photon collection window (yellow) to enable detection of fluorescence from the ensemble. This single pulse sequence is repeated over  $N_{\text{shots}}$  measurements to build up a histogram of the decay (blue). (b) Schematic of the cavity tuning mechanism in the measurement. For all of these measurements, the laser is locked to a particular frequency at the center of the ensemble's inhomogeneous distribution. This distribution is broad relative to the cavity linewidth ( $\kappa$ ) and is represented by the wide gray Lorentzian ( $\approx 17\kappa$ ). The cavity is slowly redshifted through the resonance through gas condensation tuning, and its frequency relative to the laser is given by  $\Delta_c$ . The experimental extent of  $\Delta_c$  is  $\approx 12\kappa$  as represented by the blue-to-red transition of the cavity Lorentzian. (c) Nine example experimental time traces for three different incident photon flux values ( $\phi$ ) and cavity-laser detuning values ( $\Delta_c$ ). The various black lines are fits to the experimental data as described in the main text. (d) Spontaneous decay rate enhancement ( $\Gamma/\Gamma_0$ ) as a function of the cavity-laser detuning (the x-axis is in frequency units of  $\Delta_c$  [bottom] and  $\kappa$  [top]) for increasing photon fluxes ( $\phi$ ). The  $\Gamma/\Gamma_0$  values are extracted from the stretched exponential time constants, which are fit to experimental data such as those in panel (c). The solid lines for each flux are from a pair of Lorentzian lineshapes fit to the experimental data. (e) Integration of all detected counts within collection time window for each PLE time trace with the single detuning condition of  $\Delta_c = 0.1$  GHz (the cavity is resonant with both the laser and the center of the inhomogeneous distribution) as a function incident flux, the red dashed line is a saturation fit as described in the main text.

## 2.2. Optical Measurements at 3.5 K

We perform our optical device measurements in a fiber-accessible cryostat at a sample temperature of 3.5 K, and the experimental configuration is discussed elsewhere [28]. For this work, we will explore ensemble cavity coupling to the  $Z_1 \rightarrow Y_1$  optical transition for Er in rutile phase TiO<sub>2</sub> ( $\lambda = 1520.52$  nm) [35]. We then use a continuous wave (CW) tunable laser (Toptica CTL 1550) to sweep through the device resonance and measure the reflection spectrum for the cavity. The cavity shown in [Fig. 1(c)] has a full-width half-maximum (FWHM) linewidth of  $2.94 \pm 0.05$  GHz, when centered at  $\lambda = 1520.52$  nm, and this corresponds to a  $Q = (6.71 \pm 0.11) \times 10^4$  and a waveguide-cavity mode coupling efficiency,  $\eta = 34\%$ , yielding a decay rate

from the cavity of  $\kappa_c = 0.34\kappa$ . In a simplified ambient setup with a closed-loop nanopositioner, we measure our suspended in-coupling structures to have a typical lensed fiber-to-waveguide coupling efficiency of  $\approx 75\%$ , which is close to our simulated maximum of 80%. However, when we perform the same characterization in the cryostat at 3.5 K, we see values closer to  $\approx 65\%$ .

We explore the cavity-coupled optical relaxation dynamics in these ensembles using resonant photoluminescence excitation (PLE) measurements as depicted in Fig. 2(a). We use three acousto-optic modulators (AOMs) in series to generate 5- $\mu$ s laser pulses from our tunable CW laser. After the end of the laser pulse, we wait 2  $\mu$ s before opening a fourth AOM in the

collection path to our superconducting nanowire single-photon detectors (SNSPDs), which are not gated. It should be noted that both the laser pulse length and wait time before detection are sufficiently long to allow for the fast decay of pump photons from the cavity. We can repeat each pulse sequence many times (typically  $N_{\text{shots}} = 4000$ ) to create a histogram of the ensemble fluorescence lifetime and measure the integrated intensity. Using this approach, resonant PLE from a laser sweep near 1520.52 nm yields a broad  $\text{Er}^{3+}$  ensemble linewidth of 50 GHz, as was shown previously [28], and is represented by the wide gray Lorentzian shown in Fig. 2(b). The inhomogeneous linewidth  $\Delta_{\text{inh}}$  is much broader than the cavity linewidth ( $\kappa = 2.94 \pm 0.05$  GHz), and we use nitrogen gas condensation on the cavity to tune the refractive index and slowly redshift the cavity resonance through the center of the inhomogeneous linewidth. For the majority of measurements, the laser is locked at  $\lambda = 1520.52$  nm using a wavemeter (WS-8-10, High Finesse) calibrated against a fixed frequency reference laser (SLR-1532, High Finesse). We periodically interrupt PLE measurements to perform CW laser reflection measurements, such as that shown in Fig. 1(c), to precisely measure the cavity-laser detuning parameter,  $\Delta_c$ . Given that the inhomogeneous linewidth of the  $Z_1 \rightarrow Y_1$  transition for Er in rutile  $\text{TiO}_2$  is broad, it is important to investigate if the homogeneous linewidth of these emitters is sufficiently narrow to enable cavity-based lifetime enhancement (“bad cavity” limit). Similar to previous work [28], we have performed transient spectral hole burning (TSHB) measurements at 3.5 K to find an upper bound on the homogeneous and spectral diffusion linewidths [36], as shown in Fig. S3 of [Supplement 1](#). We can see that for the range of relevant incident photon fluxes for which we see TSHB contrast, the TSHB linewidth is  $\leq 0.3$  GHz and we assume that for even higher fluxes, our cavity-coupled ensemble remains in the “bad cavity” regime.

We can now perform lifetime measurements at a variety of input laser powers for each cavity detuning. For later comparison with theory, we quantify the incident laser brightness in terms of  $\phi/\kappa$ , the photon flux given by the number of photons incident on the cavity per cavity lifetime ( $1/\kappa$ ). It is important to note that for a given detuning, we perform a full sweep of the incident fluxes and then measure the cavity reflection to gauge the resonance position. The cavity tuning rate is sufficiently slow to enable us to average our resultant lifetime histograms over five power sweeps, as this is useful in achieving sufficient detected photon numbers for the lower flux measurements, as well as averaging over fluctuations in the total intensity, as will be discussed later. As shown in Fig. 2(c), for the lowest laser power used ( $\phi = 19\kappa$ ), we measure a fast decay time close to resonance ( $\Delta_c \approx 0$ ) and slower decay at modest cavity detunings of  $\approx \pm 4$  GHz. In contrast, even though the fluorescence intensity is brighter for the highest laser power ( $\phi = 1.1 \times 10^4\kappa$ ), we see faster decay when the cavity is detuned from the transition than on resonance. Following previous work [27,28], we can fit the experimental data using a function of the form:  $A \exp[-(t/\tau_1)^d] + B \exp(-t/\tau_2) + C$ . For our case, the stretched exponential with lifetime  $\tau_1$  represents the fastest ensemble fluorescence decay rate ( $\Gamma = 1/\tau_1$ ) mediated by coupling to the cavity. The stretching exponent ( $d$ ) attempts to capture the distribution of individual ion-cavity coupling strengths ( $g$ ) within the ensemble, and the single exponential decay constant represents the much slower decay from Er ions along the inverse taper waveguide because the ions are located everywhere in the film. It is important to note that for these measurements, the

specific fit for  $\tau_1$  is robust regardless of the other parameters ( $A$ ,  $B$ ,  $d$ ,  $\tau_2$ , and  $C$ ) [28]. For increased clarity, we have included an additional plot of the dataset used in Fig. 2(c) as Fig. S5 of the SM. If we also measure the optical lifetime of the fluorescence decay rate in a bare waveguide without a cavity,  $\Gamma_0 = 1/T_1$ , where  $T_1 = 5.370 \pm 0.013$  ms (Fig. S4, SM), then the cavity-mediated Purcell enhancement,  $\Gamma/\Gamma_0$ , can be computed for each incident flux and cavity detuning, and the resultant plot is shown in Fig. 2(d). Most interesting is that at higher incident fluxes, we see a double-peak decay profile appear, and the decay rate appears to slow when the cavity is resonant with the driving field. This double-peaked detuning profile is significantly wider than the lower power cases: a single Lorentzian fit of the  $\phi = 19\kappa$  case yields a FWHM =  $3.96 \pm 0.24$  GHz, which is 35% wider than the cavity linewidth measured via reflection. However, if we integrate all photons detected at a particular detuning for each flux (regardless of time bin), the commensurate normalized intensity versus detuning plot does not show this double-lobed structure (Fig. S6, SM). Instead, all curves are qualitatively similar with comparable widths (FWHM  $\sim 5$  GHz). It is important to note that we observe this power dependence in all devices that can be tuned through the rutile Er transition, and if we probe cavities that are tuned instead to the  $\text{Er}^{3+}$  in anatase  $\text{TiO}_2$  transition (1532.6 nm), we also see very similar qualitative behavior of the lifetime decay versus detuning (Fig. S7, SM) as that shown in Fig. 2(d).

When we plot the total PLE intensity for the resonant case, as shown in Fig. 2(e), we can see the onset of saturation, where the dashed red line is a fit to a standard photoluminescence-excitation (PLE) function of the form:

$$P(\phi) = \frac{p_1}{p_2 + 1/(\phi/\kappa)}. \quad (1)$$

If we use the total experimental photon collection efficiency of our system (0.023) and the detected number of photons, we can infer  $\sim 2200$  photons generated in the cavity per pulse at the highest pump power ( $\phi = 1.1 \times 10^4\kappa$ ). Since we are in a saturation regime, we can generally conclude that the number of ions that are addressed with our optical pulse is close to this value. Using our device geometry and doping density, we very coarsely estimate that there are  $7 \times 10^4$  total ions along the cavity, though our uncertainty is quite large given the unknown proportion of Er ions residing in the rutile versus anatase grains. However, if we use this value and make another coarse estimate that if the spectral window that is being addressed with these highest power pulses is approximately the cavity linewidth ( $\kappa = 2.94$  GHz), then we expect  $\sim 2600$  ions to couple. Since our estimates on ion number and photons generated in the cavity are reasonably close (in a regime where the ensemble appears to be saturating), we expect that the number of participating ions is close to 2000, and this estimate is useful in conducting simulations to explain the features in the Purcell factor detuning dependence.

### 3. THEORY AND DISCUSSION

#### 3.1. Semiclassical Model

To model the interaction between the nanophotonic cavity and the Er ions coupled to it, we treat each ion as a two-level system, representing the  $Z_1$  and  $Y_1$  levels, which is interacting with the

cavity mode via a standard Tavis–Cummings interaction,

$$\hat{H} = \Delta_c \hat{a}^\dagger \hat{a} + \sum_{j=1}^N \delta_j \frac{\hat{\sigma}_z^j}{2} + \sum_{j=1}^N g_j (\hat{a}^\dagger \hat{\sigma}_-^j + \hat{a} \hat{\sigma}_+^j) - i\sqrt{\kappa_c} \beta_{\text{in}} (\hat{a}^\dagger - \hat{a}). \quad (2)$$

Here,  $\hat{\sigma}_z^j$  is the Pauli  $z$  matrix of ion  $j$ ,  $\hat{\sigma}_\pm^j$  are the associated spin raising and lowering operators, respectively, and  $\hat{a}$  is the lowering operator of the cavity mode. The cavity is driven by a laser at frequency  $\omega_{\text{dr}}$  which generates an input photon flux  $\phi = |\beta_{\text{in}}|^2$ . We work in a frame rotating at the drive frequency and  $\Delta_c = \omega_c - \omega_{\text{dr}}$  ( $\delta_j = \omega_j - \omega_{\text{dr}}$ ) is the corresponding detuning of the cavity (ion  $j$ ). Relaxation of each ion and damping of the cavity are described by the quantum master equation:

$$\frac{d}{dt} \hat{\rho} = -i [\hat{H}, \hat{\rho}] + \kappa \mathcal{D}[\hat{a}] \hat{\rho} + \gamma \sum_{j=1}^N \mathcal{D}[\hat{\sigma}_-^j] \hat{\rho}, \quad (3)$$

where  $\mathcal{D}[\hat{\rho}] \hat{\rho} = \hat{\rho} \hat{\rho} \hat{\rho}^\dagger - \{\hat{\rho}^\dagger \hat{\rho}, \hat{\rho}\}/2$  is a Lindblad dissipator. Here,  $\gamma$  is the relaxation rate of the ions and  $\kappa$  is the total cavity damping rate, which accounts for the damping rate  $\kappa_c$  due to the input port (through which the drive laser enters the cavity) and other internal losses.

Since it is intractable to solve the quantum master equation, Eq. (3), for large ensembles of ions, we derive equations of motion for the coherent cavity field  $a = \langle \hat{a} \rangle$ , as well as the spin populations  $s_z^j = \langle \hat{\sigma}_z^j \rangle$  and coherences  $s_-^j = \langle \hat{\sigma}_-^j \rangle$ . Because of the nonlinearity of the spins, these equations of motion will not form a closed set of differential equations. We therefore perform a semiclassical approximation  $\langle \hat{\sigma}_1 \hat{\sigma}_2 \rangle \approx \langle \hat{\sigma}_1 \rangle \langle \hat{\sigma}_2 \rangle$  [37], also known as a first-order mean-field approximation, which leads to

$$\frac{d}{dt} a = - \left( i\Delta_c + \frac{\kappa}{2} \right) a - i \sum_{j=1}^N g_j s_-^j - \sqrt{\kappa_c} \beta_{\text{in}}, \quad (4)$$

$$\frac{d}{dt} s_-^j = - \left( i\delta_j + \frac{\gamma}{2} \right) s_-^j + i g_j a s_z^j, \quad (5)$$

$$\frac{d}{dt} s_z^j = 2 i g_j [a^* s_-^j - a(s_-^j)^*] - \gamma(1 + s_z^j). \quad (6)$$

Even though this approximation neglects all correlations between the cavity field and the spins and does not take into account the presence of the ions coupled to the inverse taper, the resulting equations of motion are still able to capture the relevant qualitative aspects of the experimental data, as we will show below.

To simulate the dynamics of a disordered ensemble of ions, we randomly draw the detunings  $\delta_j$  of  $N - 1$  ions from a Lorentzian distribution  $L(\delta, \tilde{\delta}, h) = h/\pi[(\delta - \tilde{\delta})^2 + h^2]$ , centered around  $\tilde{\delta} = 0$  with an FWHM of  $2h = \Delta_{\text{inh}}$ . The remaining last ion is always chosen to be resonant with the drive. Similarly, we randomly draw the coupling strengths  $g_j$  of each ion from a Gaussian distribution  $G(g, \bar{g}, \sigma) = \exp[-(g - \bar{g})^2/2\sigma^2]/\sqrt{2\pi}\sigma$  with mean coupling strength  $\bar{g}$  and standard deviation  $\sigma$ . This procedure ensures that the detunings  $\delta_j$  and the couplings  $g_j$  of each ion are uncorrelated random variables. Since a finite number of spins is in general not sufficient to smoothly sample a broad inhomogeneous frequency distribution, we repeat this procedure  $n_{\text{traj}}$  times to generate a set of random disorder realizations. For each of these disorder realizations, we initialize the cavity in the vacuum state and the ions in the ground state, i.e.,  $a = s_z^j = 0$  and  $s_-^j = -1$ , and evolve the semiclassical equations of motion, Eqs. (4)–(6), with the laser drive switched on,  $\beta_{\text{in}} > 0$ ,

for a time  $t_{\text{pulse}}$ . Subsequently, we use the final state at  $t_{\text{pulse}}$  as the new initial state for a simulation of the fluorescence of the ion ensemble, where the laser drive has been switched off,  $\beta_{\text{in}} = 0$ . The semiclassical output field of the cavity is  $a_{\text{out}} = \sqrt{\kappa_c} a + \beta_{\text{in}}$ , and the photon flux impinging on a photodetector measuring the output mode is  $|a_{\text{out}}|^2$ .

For the numerical simulations, we choose parameters that are inspired by the corresponding experimental values but allow us to perform efficient simulations of the inhomogeneously broadened spin ensemble. Based on the transient-spectral-hole-burning experiments, we choose the spin decay rate to be  $\gamma = 0.005\kappa$ . To get a larger output mode amplitude, we increase the output coupling strength compared with the experimental value and use  $\kappa_c = 0.8\kappa$ . We reduce the width of the inhomogeneous distribution to  $\Delta_{\text{inh}} = 5\kappa$  to be able to perform disorder averages using  $N = 61$  ions and  $n_{\text{traj}} = 120$  random disorder realizations. Since the experimental value of the coupling strength of the ions is unknown, we choose  $\bar{g} = 0.07\kappa$  and  $\sigma = 0.01\kappa$ , such that  $C = 4N\bar{g}^2/\kappa\gamma \gg 1$  should allow us to resolve collective effects in the simulations of a disorder-free ensemble. Note that the presence of inhomogeneous broadening leads to a modified cooperativity  $C_{\text{inh}}$  (defined below), which is only approaching unity.

### 3.2. Explicit Form of the State Prepared by Excitation Pulse

The state of the ion ensemble at the end of the excitation pulse can be well understood using an argument that combines single-spin (i.e., local) dynamics and the concept of collectively induced transparency (CIT), which has recently been introduced and experimentally demonstrated [27]. For an excitation pulse that is long compared with both the cavity decay timescale  $1/\kappa$  and the intrinsic spin decay timescale  $1/\gamma$ , the system will approach a drive-dependent steady state. After eliminating the spin coherence  $s_-^j$  by solving for the steady state of Eq. (5), one finds that the steady-state cavity field and the spin excitations are given by the self-consistent solution of

$$a_{\text{ss}} = \frac{i\sqrt{\kappa_c} \beta_{\text{in}}}{\Delta_c - i\frac{\kappa}{2} + \sum_{j=1}^N \frac{g_j^2}{\delta_j - i\gamma/2} s_z^j}, \quad (7)$$

$$s_z^j_{\text{ss}} = - \left( 1 + \frac{2g_j^2}{\delta_j^2 + \gamma^2/4} |a_{\text{ss}}|^2 \right)^{-1}. \quad (8)$$

The last term in the denominator of Eq. (7) represents a spin-excitation-dependent self energy that can renormalize both the effective detuning  $\Delta_c$  and the decay rate  $\kappa$  of the cavity. In the limit of weakly excited spins,  $s_z^j \approx -1$ , Eq. (7) can be averaged over the disorder distributions  $L(\delta, 0, \Delta_{\text{inh}}/2)$  and  $G(g, \bar{g}, \sigma)$ ,

$$\bar{a}_{\text{ss}} = \frac{i\sqrt{\kappa_c} \beta_{\text{in}}}{\Delta_c - i \left[ \frac{\kappa}{2} + \frac{2N_{\text{eff}}(\bar{g}^2 + \sigma^2)}{\gamma + \Delta_{\text{inh}}} \right]}, \quad (9)$$

i.e., the disorder-averaged self energy is purely imaginary and merely renormalizes the cavity decay rate. Here,  $N_{\text{eff}} < N$  is the effective number of ions in the ensemble that contribute to the sum in Eq. (7), i.e., those ions that have not been depolarized into a state with  $s_z^j \approx 0$ . These results also reveal that the relevant collective cooperativity that controls renormalizations of the bare cavity damping rate  $\kappa$  due to its interaction with the spin ensemble is  $C_{\text{inh}} = 4N_{\text{eff}}\bar{g}^2/\Delta_{\text{inh}}\kappa$ , where we assumed  $\sigma^2 \ll \bar{g}^2$

and  $\gamma \ll \Delta_{\text{inh}}$ . Even though the collective cooperativity  $C$  may be large,  $C_{\text{inh}} \approx 0.24$  is only modest due to the large inhomogeneous broadening  $\Delta_{\text{inh}}$ . Surprisingly, this result provides an excellent description of the disorder-averaged steady-state cavity field even in the limit of strong driving, where spins resonant with the drive laser are almost depolarized,  $s_z^j \rightarrow 0$ . An intuitive explanation is the CIT effect [27]. For  $|\bar{a}_{ss}|g_j \gg \gamma$ , ions in a window  $|\delta_j| \ll |\bar{a}_{ss}|g_j$  around the drive laser frequency will be highly depolarized,  $s_z^j \approx 0$ , and their contributions to the self energy term in Eq. (7) will be suppressed. Consequently, the self energy will be dominated by spins with a large detuning  $|\delta_j| \gg |\bar{a}_{ss}|g_j$ , but these spins have  $s_z^j \approx -1$  such that the weak-drive assumption used to derive Eq. (9) remains valid if  $N_{\text{eff}}$  is suitably adjusted. For our numerical parameters, the renormalization of the cavity decay rate by the self-energy term is less than 24% due to the small value of  $C_{\text{inh}}$ .

Given the analytical expression in Eq. (9), we decompose the cavity field into its semiclassical disorder-averaged steady-state value and quantum fluctuations  $\hat{d}$ ,  $\hat{a} = \bar{a}_{ss} + \hat{d}$ , and find that, to leading order,  $\hat{H}$  decouples into a sum of  $N$  independent single-spin Hamiltonians  $\hat{H}_j = \delta_j \hat{\sigma}_z^j/2 + g_j(\bar{a}_{ss}^* \hat{\sigma}_-^j + \bar{a}_{ss} \hat{\sigma}_+^j)$ , each describing a coherent Rabi drive. This Rabi drive competes with single-spin relaxation and detuning  $\delta_j$  such that each spin relaxes to a steady state with

$$s_{z,ss}^j = -1 + \frac{8|\bar{a}_{ss}|^2 g_j^2}{8|\bar{a}_{ss}|^2 g_j^2 + \gamma^2 + 4\delta_j^2}, \quad (10)$$

$$s_{-,ss}^j = -\frac{2\bar{a}_{ss}g_j}{8|\bar{a}_{ss}|^2 g_j^2 + \gamma^2 + 4\delta_j^2}(i\gamma + 2\delta_j). \quad (11)$$

These expressions agree very well with the corresponding quantities obtained from a numerical solution of the semiclassical equations of motion in Eqs. (4)–(6).

### 3.3. Fluorescence Decay Rate

We now analyze the fluorescent decay of the initial state given by Eqs. (7), (10), and (11). Since the laser drive is switched off during the fluorescence measurement, the disorder-averaged fluorescence signal is given by

$$\overline{F(t)} = \overline{\kappa_c |a|^2} = \frac{1}{n_{\text{traj}}} \sum_{k=1}^{n_{\text{traj}}} \kappa_c |a^{(k)}(t)|^2, \quad (12)$$

where  $a^{(k)}(t)$  denotes the cavity field calculated numerically for the disorder realization  $k \in \{1, \dots, n_{\text{traj}}\}$ . Examples of the simulated fluorescence curves are shown in Fig. 3(a) and display two different regimes. Immediately after the end of the laser pulse, at time  $t_{\text{pulse}}$ , the cavity is still populated with photons generated by the laser drive. These photons decay out of the cavity for times  $t - t_{\text{pulse}} \lesssim 10/\kappa$ . Because we wait 2  $\mu\text{s}$  before opening the collection AOM, this regime is not observable in the experiments. At much longer times  $t - t_{\text{pulse}} \gg 10/\kappa$ , the fluorescence is dominated by slow emission from the spin ensemble. This regime corresponds to the experimental measurements shown in Figs. 2(c) and 2(d). To extract the relaxation rate of  $\overline{F(t)}$  in this regime, we fit the numerically obtained fluorescence data to an exponential decay  $ce^{-\Gamma(t-t_{\text{pulse}})}$  with free parameters  $c$  and  $\Gamma$ .

The ratio between the spontaneous decay rate  $\Gamma$  and the cavity decay rate  $\kappa$  is shown in Fig. 3(b). Despite the fact that we approximate the full quantum dynamics with a semiclassical model and ignore the presence of Er ions coupled to the

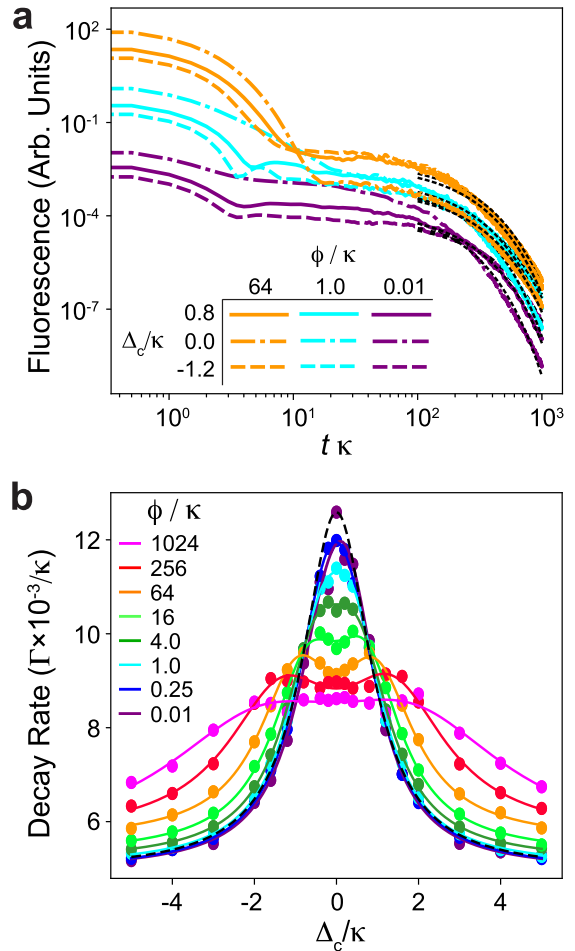


**Fig. 3.** Simulated PLE measurements on cavity-coupled Er ensembles, based on the semiclassical model of the relaxation dynamics given by Eqs. (4)–(6). (a) Nine examples of the disorder-averaged fluorescence  $\overline{F(t)}$ , defined in Eq. (12), for three different incident photon-flux values ( $\phi = |\beta_{\text{in}}|^2$ ) and cavity-laser detuning values  $\Delta_c$ . The various dotted black lines are exponential fits  $c \exp(-\Gamma t)$  to the decay dynamics for  $t \gg 1/\kappa$ . (b) Spontaneous decay rate relative to the cavity decay rate ( $\Gamma/\kappa$ ) as a function of the cavity-laser detuning ( $\Delta_c$ ) for increasing photon flux values ( $\phi$ ). The error bars of the fitted decay rates are smaller than the plot markers. The solid lines for each flux are double Lorentzian fits to the simulated data. The dashed black line is a single Lorentzian function with FWHM  $2\kappa$ .

bus waveguide, the spontaneous decay rate qualitatively reproduces the experimental measurements shown in Fig. 1(d). At the smallest input flux  $\phi = 0.01\kappa$ , the spontaneous decay rate is maximum on resonance,  $\Delta_c = 0$  and decreases for finite cavity detuning according to a Lorentzian function whose FWHM is given by  $2\kappa$ ,  $L(\Delta_c, 0, \kappa)$  [dashed black curve in Fig. 3(b)]. This is in rough agreement with our experimental findings where the Lorentzian lineshape of the Purcell enhanced decay rate is  $\approx 35\%$  wider than the cavity linewidth as determined from reflection scans. At a slightly larger input flux of  $\phi = 0.25\kappa$ , the curve of the decay rate shows a flat region around zero detuning, which is consistent with the curve being the sum of two detuned Lorentzian functions. This interpretation also lets us understand the behavior at higher fluxes  $\phi \gtrsim 16\kappa$ , where one

sees two distinct local maxima at finite detuning  $|\Delta_c| > 0$ . The separation of these new maxima increases with drive power and ultimately exceeds  $2\kappa$ . At the same time, the decay rate for a resonant cavity decreases.

To quantify the separation between the two Lorentzian functions, we fit the decay rate to  $a[L(\Delta_c, \Delta_+, h_+) + L(\Delta_c, \Delta_-, h_-)] + b$ . Free parameters are the overall amplitude  $a$ , the offset  $b$ , the detunings  $\Delta_{\pm}$  of the two peaks, and the corresponding width parameters  $h_{\pm}$ . These fits are shown by the solid lines in Fig. 3(b). In Fig. S9 of the SM, we compare the experimental results shown in Fig. 2(d) with their simulated equivalents shown in Fig. 3(b) using two figures of merit: the splitting  $\Delta_+ - \Delta_-$  extracted from the Lorentzian fits and the ratio between the maximum decay rate  $\Gamma$  at a given input flux  $\phi$ ,  $\max_{\Delta_c}(\Gamma|_{\phi})$ , and its corresponding value at the smallest input flux  $\phi_{\min}$ ,  $\max_{\Delta_c}(\Gamma|_{\phi_{\min}})$ . In both cases, we find that the semiclassical model agrees with the experimental data for  $\phi \ll \phi_0$ , where  $\phi_0$  is the critical flux above which saturation effects start to become relevant (see SM for further details). Larger deviations between the semiclassical and the experimental data emerge when entering the saturation regime  $\phi \gg \phi_0$ . We attribute this effect to the different values of the inhomogeneous broadening  $\Delta_{\text{inh}}$  in the experiment and the simulations. Intuitively,  $\Delta_{\text{inh}}$  determines the spectral extent of the ion ensemble and defines an upper bound on the maximum possible splitting  $\Delta_+ - \Delta_-$ . Due to the smaller value of  $\Delta_{\text{inh}}$ , these finite size effects of the ion ensemble will be more pronounced in the simulations.

### 3.4. Anomalous Spin Relaxation and Toy Model of the Decay Dynamics

Both the experimental data and the semiclassical simulations exhibit a striking transition from a weak-drive regime where  $\Gamma$  decays monotonically with increasing  $|\Delta_c|$  [i.e., a single peak in the optical decay rate versus  $|\Delta_c|$ , c.f., Figs. 2(d) and 3(b)] to a high-drive regime where  $\Gamma$  is non-monotonic with increasing  $|\Delta_c|$  (i.e., two symmetric peaks in  $\Gamma$  at nonzero cavity detunings). As we now discuss, the simulations provide insight into this phenomenon, as they show that a similar transition occurs if we look at the frequency-resolved decay of different spins in our ensemble.

To understand how spins with a certain detuning  $\delta_j$  from the drive laser decay, we employ a binning procedure. For each disorder realization, we assign each spin to a frequency bin of width  $0.167\kappa$  based on their random detuning  $\delta_j$ . Averaging over many realizations, we can then compute the average time-dependent spin excitation  $1 + s_z^j$  in each frequency-resolved bin. We present results for the case  $\Delta_c = 0$  in the SM. Surprisingly, we find that for sufficient drive strengths, spins that are resonant with the cavity ( $\delta_j \approx \Delta_c = 0$ ) decay far slower than spins with a large detuning (see Fig. S10, SM). While this feature cannot be probed in the current experiment, it could be measured by analyzing the frequency-resolved fluorescence using a narrow spectral filter. The slow decay of resonant spins is at odds with the naive expectation that the Purcell effect enhances the relaxation of resonant spins, which should therefore decay faster than detuned spins. To provide an intuitive explanation of this effect, and to understand the aforementioned non-monotonicity of the decay rate at large fluxes, we now derive and analyze a simple toy model that captures the essential physics of the spin relaxation process.

The key observation is that the steady-state spin coherence at

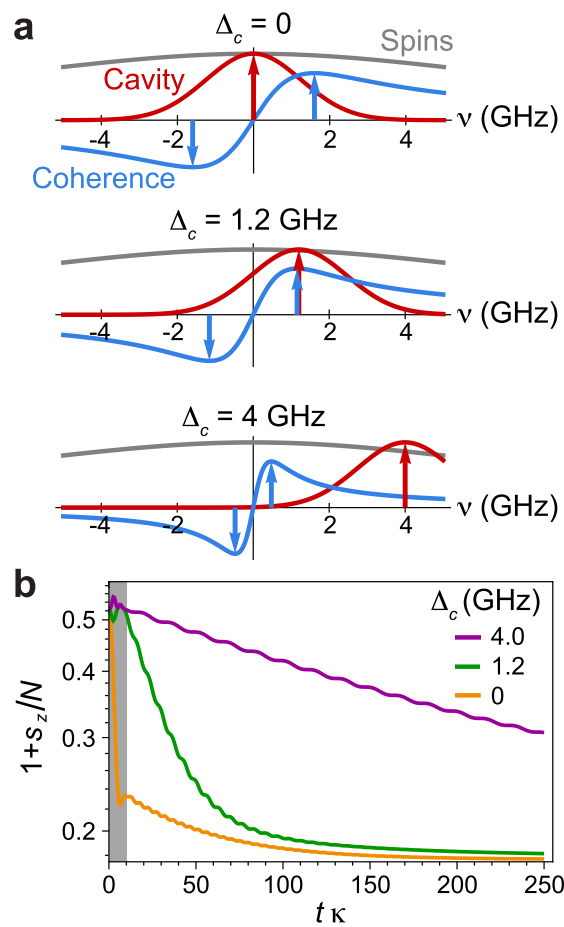


**Fig. 4.** Mechanism for non-monotonicity via toy three-spin model. (a) Plot of the inhomogeneously broadened spin distribution [using a Lorentzian with half-width at half-maximum  $\Delta_{\text{inh}} = 10$  GHz (gray)], the cavity linewidth for  $\kappa = 2.5$  GHz (red) and the steady-state spin coherence  $s_{-ss}^j$  for a spin detuning at corresponding frequency  $\nu = \delta_j$  (blue), plotting just the real part for clarity. The vertical axis is in arbitrary unscaled units for all curves. Vertical arrows demonstrate a toy model coarse-graining the ensemble into three large spins. These include one resonant spin  $s^0$  and two off-resonant spins  $s^{L/R}$  with detunings  $-\delta_S, +\delta_S$  at the points where spin coherence is maximal, given by  $\delta_S = \sqrt{2g|\bar{a}_{ss}|}$  for a fixed input flux  $\phi/\kappa = 4,000$ . (b) Decay dynamics of total spin excitation  $s_z = s_z^L + s_z^0 + s_z^R$  for this toy model, normalized by total ion number  $N = N^0 + N^L + N^R$ . The spin sizes are  $N^0 = 100$ ,  $N^{L/R} = 1,000$ , and the parameters are  $g = 4 \times 10^{-3}\kappa$ ,  $\gamma = 0$  (set to zero to emphasize the transient Purcell-enhanced features). One sees that the effective decay rate of excitations has a non-monotonic dependence with  $\Delta_c$ , and is strongest when the cavity is resonant with the spins with largest coherence. The shaded region corresponds to short times  $t\kappa \leq 10$  during which initial photons built up in the cavity by the pulse leak out.

the end of the laser pulse, Eq. (11), is non-monotonic as a function of spin detuning  $\delta_j$ . Resonant spins have zero coherence,  $s_{-ss}^j(\delta_j = 0) \approx 0$ , due to the interplay between local decay and the Rabi drive generated by the cavity field. Similarly, the coherence of highly detuned spins tends to zero,  $s_{-ss}^j(|\delta_j| \rightarrow \infty) \rightarrow 0$ , as they remain in the ground state. At intermediate detunings, however, there is a group of spins whose coherence is non-negligible. We argue that it is precisely these detuned spins

that contribute to the higher Purcell enhancement of fluorescence at intermediate cavity detuning  $\Delta_c$ . The core idea is visualized in Fig. 4(a), which shows the steady-state spin coherence  $s_{-,ss}^j$  in frequency space for a fixed large input flux  $\phi/\kappa$  after the laser pulse. The cavity linewidth and the broad spin distribution are also shown on the same horizontal axis. At the level of semiclassics, when the cavity is at resonance  $\Delta_c = 0$ , the spins with which it is resonant have no coherence, hence they cannot coherently exchange excitations. As the cavity is shifted to finite detuning  $\Delta_c$ , it instead becomes resonant with spins that have non-negligible coherence, which permits photon exchange and enables Purcell decay. Going further to the limit  $\Delta_c \rightarrow \infty$  again leads to spins which lack coherence, and eventually a lack of spins once the edge of the spin distribution is reached.

To simplify the physics behind this mechanism, we coarse-grain the inhomogeneous spin ensemble, replacing it with just three large collective spins depicted by the arrows in Fig. 4(a). One spin (size  $N^0$ ) is resonant with the spin transition and represents spins that are depolarized by the laser pulse, with spin operators  $s_\alpha^0$  for  $\alpha \in \{+, -, z\}$ . The other two spins (sizes  $N^L = N^R$ ) are taken to have equal and opposite fixed detunings  $\pm\delta_S$ , representing the set of spins off-resonant from the transition with maximal nonzero coherence, with spin operators  $s_\alpha^L$ ,  $s_\alpha^R$ . This characteristic detuning is chosen to be precisely at the maximum of  $s_{-,ss}^j$ . The location of the maximum is  $\delta_S \approx \sqrt{2}g|\bar{a}_{ss}|$  with  $\bar{a}_{ss}$  the cavity field following the pulse from Eq. (9), neglecting the spin contributions in the denominator for simplicity (see SM for further details). Note that this  $\delta_S$  is not fixed, but increases for stronger laser power (larger  $\phi$ ) and decreases with cavity detuning (since this leads to a smaller  $|\bar{a}_{ss}|$ ). By choosing  $(N^L = N^R) \gg N^0 \gg 1$ , we can use this toy model of three large spins to qualitatively capture key aspects of the full ensemble. This hierarchy of spin sizes reflects the fact that there are many detuned spins with near optimal initial coherence (see SM for further details). Note that this toy model relies upon the ensemble being inhomogeneously broadened, and breaks down once the characteristic detuning  $\delta_S$  becomes larger than the width of the ensemble frequency distribution.

The relaxation dynamics for such a three-spin system is solved semi-classically, with initial conditions equivalent to the steady-state solutions of the laser-driven full ensemble. The cavity field is initialized to  $a(0) = \bar{a}_{ss}$  for a fixed value of  $\phi/\kappa$ . The spins are initialized to  $s_\alpha^{0,L,R} = N^{0,L,R} s_{\alpha,ss}^{0,L,R}$  from Eqs. (10) and (11), with  $\delta_{0,L,R} = 0, -\delta_S, +\delta_S$ , respectively.

Figure 4(b) plots the relaxation dynamics of the total spin excitation fraction  $s_z = s_z^L + s_z^0 + s_z^R$  in this toy model, using similar parameters as the ensemble semiclassical simulations (see Fig. 3) for a strong initial laser pulse. We find that past a short transient interval  $t\kappa \sim 1$  (during which photons in the cavity left over from the pulse leak out), there is a strong non-monotonic behavior in the excitation decay rate. The decay is fastest for intermediate cavity detuning  $\Delta_c$  that precisely corresponds to the point at which the cavity is resonant with one of the large spins, as shown in Fig. 4(a). At this intermediate detuning, excitations are extracted most efficiently from the off-resonant spins with coherence, here captured by a single large spin. The complementary other large spin at negative detuning would instead contribute to enhanced decay for equal and opposite  $\Delta_c$ . The broad inhomogeneous distribution of the spins relative to the cavity plays a crucial role in this physics; as seen from Fig. 4(a),

if the spin distribution was narrower than the cavity, such non-monotonic features would not be resolvable as there would be no spins left at the key characteristic detunings at which coherence is non-negligible.

We note that most of the decay physics can be understood from just the off-resonant spins, and does not need to involve a third one at zero detuning. Depolarized spins at the transition resonance do not strongly contribute to the non-monotonic decay features since most of the spins are off-resonant, due to strong inhomogeneous broadening. Nonetheless, on more general theoretical grounds, it is interesting to note that the long survival of resonant spins found in the semi-classical simulations can also be understood from the picture in Fig. 4. At the level of semiclassics, the central non-detuned spin on its own cannot have any cavity-mediated Purcell decay because it is depolarized (and hence has no coherence,  $s_-^0 \approx 0$ ), which prevents it from coherently trading excitations with the cavity. It will simply undergo intrinsic loss at rate  $\gamma$ . However, as the intermediate-detuned spins with coherence leak into the cavity, they generate a transient field. This field drives the resonant spins and keeps them excited, preventing even intrinsic decay, provided that the off-resonant Purcell decay is still ongoing (see SM for further details). While the present experiment may not be sensitive to such features directly, they can be resolved with future upgrades, and represent an interesting physical effect exclusive to frequency-broadened ensembles.

#### 4. CONCLUSION

In this work, we have used an inhomogeneously broadened ensemble of Er ions evanescently coupled to a relatively narrow optical nanocavity to explore optical decay dynamics as a function of laser-cavity detuning and pump power. To realize these measurements, we developed a materials-compatible nanofabrication process to greatly improve the device-to-fiber photon collection efficiency. Our resonant PLE measurements reveal an interesting three-fold suppression of the Purcell-enhanced optical lifetime at the highest pump fluence measured when the cavity is resonant with the optical transition. We estimate that the number of ions participating in this effect is roughly 2000 at the highest incident photon flux. We have employed a semiclassical model that captures qualitative aspects of the experimental optical relaxation even with a modest number of  $N = 61$  ions.

From these simulations, there appear to be rich decay dynamics that happen in the time regime between traditional cavity photon and spin decay processes ( $\sim 1/\kappa < t < 1/\Gamma$ ) that are not being accessed in the current experimental configuration. In the future, it would be beneficial to switch to gated operation of single-photon detectors that can simultaneously enable higher collection efficiency by removal of a lossy modulator in the collection path and detection of photons earlier in the relaxation process. In addition, there are likely other interesting dynamics that occur as the photons impinge and reflect from the cavity, as has been explored recently in the regime of spectrally narrower but larger ensembles of ions coupled to lower Q cavities [27]. In future experiments, it would be interesting to use an ultra-narrowband optical filter to spectrally distinguish differences in the emitter contribution of collected PLE emission.

From a modeling perspective, it would be beneficial to optimize the numerical implementation to investigate these effects in larger ensembles that approach the experimental number of

ions probed. A much larger simulated ensemble size can enable us to modify other parameters to better emulate experimental conditions, such as increasing the ensemble inhomogeneous linewidth, reducing the cavity-waveguide coupling efficiency  $\kappa_c$ , and broadening the disorder averaged ion-cavity coupling strength. In doing so, we may be able to reduce potential finite-size effects in the splitting of the peak decay rates as a function of  $\phi$  to better match experimental results. On the theory side, an analytical understanding of the emergence of the double-peaked structure in the fluorescence decay rate is desired, and such insights would provide clarity on the origin of the surprising survival of excitations in spins that are resonant with the cavity mode.

Both our experimental measurements and modeling may have ramifications for applications involving quantum memories. From our calculations, far-detuned emitters can have coherence if they are not completely depolarized by the laser drive, which means they can store quantum superposition information. Thus, the system has applications as a generalized quantum memory, where coherence can be stored and extracted when needed. More practically for researchers exploring frequency-multiplexed quantum memories (e.g., frequency addressable individual rare-earth ions within an ensemble) coupled to the same nanocavity, our results have shown that the cavity can still couple detuned emitters together depending on detailed cavity resonance and excitation conditions. This may have an impact on multiplexed memory protocols, and further studies accounting for the cavity-mediated interactions across the ion frequency distribution will be useful moving forward.

**Funding.** Office of Science (DE-FOA-582 000225, Q-NEXT Quantum Center); Basic Energy Sciences (Materials Science and Engineering Division).

**Acknowledgments.** All electron microscopy and device fabrication were performed at the Center for Nanoscale Materials, a U.S. Department of Energy Office of Science User Facility, supported by the U.S. DOE, Office of Basic Energy Sciences, under Contract No. DE-AC02-06CH11357. The authors would like to thank D. Czaplewski, C. S. Miller, and R. Divan for assistance with device fabrication.

**Disclosures.** The authors declare no conflicts of interest.

**Data availability.** Data underlying the results presented in this paper are not publicly available at this time but may be obtained from the authors upon reasonable request.

**Supplemental document.** See Supplement 1 for supporting content.

## REFERENCES

- K. Hammerer, A. S. Sørensen, and E. S. Polzik, "Quantum interface between light and atomic ensembles," *Rev. Mod. Phys.* **82**, 1041–1093 (2010).
- A. Reiserer and G. Rempe, "Cavity-based quantum networks with single atoms and optical photons," *Rev. Mod. Phys.* **87**, 1379–1418 (2015).
- E. M. Purcell, H. C. Torrey, and R. V. Pound, "Resonance absorption by nuclear magnetic moments in a solid," *Phys. Rev.* **69**, 37–38 (1946).
- H. Walther, B. T. H. Varcoe, B.-G. Englert, *et al.*, "Cavity quantum electrodynamics," *Rep. Prog. Phys.* **69**, 1325–1382 (2006).
- E. Jaynes and F. Cummings, "Comparison of quantum and semiclassical radiation theories with application to the beam maser," *Proc. IEEE* **51**, 89–109 (1963).
- R. H. Dicke, "Coherence in spontaneous radiation processes," *Phys. Rev.* **93**, 99–110 (1954).
- M. Gross and S. Haroche, "Superradiance: an essay on the theory of collective spontaneous emission," *Phys. Rep.* **93**, 301–396 (1982).
- V. V. Temnov and U. Woggon, "Superradiance and subradiance in an inhomogeneously broadened ensemble of two-level systems coupled to a low-Q cavity," *Phys. Rev. Lett.* **95**, 243602 (2005).
- M. A. Norcia, R. J. Lewis-Swan, J. R. K. Cline, *et al.*, "Cavity-mediated collective spin-exchange interactions in a strontium superradiant laser," *Science* **361**, 259–262 (2018).
- Z. Kurucz, J. H. Wesenberg, and K. Mølmer, "Spectroscopic properties of inhomogeneously broadened spin ensembles in a cavity," *Phys. Rev. A* **83**, 053852 (2011).
- B. Julsgaard and K. Mølmer, "Dynamical evolution of an inverted spin ensemble in a cavity: Inhomogeneous broadening as a stabilizing mechanism," *Phys. Rev. A* **86**, 063810 (2012).
- B. Julsgaard and K. Mølmer, "Fundamental limitations in spin-ensemble quantum memories for cavity fields," *Phys. Rev. A* **88**, 062324 (2013).
- M. Blaha, A. Johnson, A. Rauschenbeutel, *et al.*, "Beyond the Tavis-Cummings model: revisiting cavity QED with ensembles of quantum emitters," *Phys. Rev. A* **105**, 013719 (2022).
- J. D. Thompson, T. G. Tiecke, N. P. de Leon, *et al.*, "Coupling a single trapped atom to a nanoscale optical cavity," *Science* **340**, 1202–1205 (2013).
- J. Gallego, W. Alt, T. Macha, *et al.*, "Strong Purcell effect on a neutral atom trapped in an open fiber cavity," *Phys. Rev. Lett.* **121**, 173603 (2018).
- A. Kumar, A. Suleymanzade, M. Stone, *et al.*, "Quantum-enabled millimetre wave to optical transduction using neutral atoms," *Nature* **615**, 614–619 (2023).
- H. Mabuchi, J. Ye, and H. J. Kimble, "Full observation of single-atom dynamics in cavity QED," *Appl. Phys. B: Lasers Opt.* **68**, 1095–1108 (1999).
- A. Goban, C.-L. Hung, J. D. Hood, *et al.*, "Superradiance for atoms trapped along a photonic crystal waveguide," *Phys. Rev. Lett.* **115**, 063601 (2015).
- D. E. Chang, J. S. Douglas, A. González-Tudela, *et al.*, "Colloquium: quantum matter built from nanoscopic lattices of atoms and photons," *Rev. Mod. Phys.* **90**, 031002 (2018).
- M. Mirhosseini, E. Kim, X. Zhang, *et al.*, "Cavity quantum electrodynamics with atom-like mirrors," *Nature* **569**, 692–697 (2019).
- J. M. Kindem, A. Ruskuc, J. G. Bartholomew, *et al.*, "Control and single-shot readout of an ion embedded in a nanophotonic cavity," *Nature* **580**, 201–204 (2020).
- M. Raha, S. Chen, C. M. Phenicie, *et al.*, "Optical quantum nondemolition measurement of a single rare earth ion qubit," *Nat. Commun.* **11**, 1605 (2020).
- S. Chen, M. Raha, C. M. Phenicie, *et al.*, "Parallel single-shot measurement and coherent control of solid-state spins below the diffraction limit," *Science* **370**, 592–595 (2020).
- S. Ourari, Ł. Dusanowski, S. P. Horvath, *et al.*, "Indistinguishable telecom band photons from a single Er ion in the solid state," *Nature* **620**, 977–981 (2023).
- T. Xie, J. Rochman, J. G. Bartholomew, *et al.*, "Characterization of Er<sup>3+</sup>:YVO<sub>4</sub> for microwave to optical transduction," *Phys. Rev. B* **104**, 054111 (2021).
- J. Rochman, T. Xie, J. G. Bartholomew, *et al.*, "Microwave-to-optical transduction with erbium ions coupled to planar photonic and superconducting resonators," *Nat. Commun.* **14**, 1153 (2023).
- M. Lei, R. Fukumori, J. Rochman, *et al.*, "Many-body cavity quantum electrodynamics with driven inhomogeneous emitters," *Nature* **617**, 271–276 (2023).
- A. M. Dibos, M. T. Solomon, S. E. Sullivan, *et al.*, "Purcell enhancement of erbium ions in TiO<sub>2</sub> on silicon nanocavities," *Nano Lett.* **22**, 6530–6536 (2022).
- C. Ji, M. T. Solomon, G. D. Grant, *et al.*, "Nanocavity-mediated Purcell enhancement of Er in TiO<sub>2</sub> thin films grown via atomic layer deposition," *ACS Nano* **18**, 9929–9941 (2024).
- M. K. Singh, A. Prakash, G. Wolfowicz, *et al.*, "Epitaxial Er-doped Y<sub>2</sub>O<sub>3</sub> on silicon for quantum coherent devices," *APL Mater.* **8**, 031111 (2020).

31. K. Shin, I. Gray, G. Marcaud, *et al.*, "Er-doped anatase TiO<sub>2</sub> thin films on LaAlO<sub>3</sub> (001) for quantum interconnects (QuICs)," *Appl. Phys. Lett.* **121**, 081902 (2022).
32. M. K. Singh, G. Wolfowicz, J. Wen, *et al.*, "Development of a scalable quantum memory platform – materials science of erbium-doped TiO<sub>2</sub> thin films on silicon," *arXiv*, arXiv:2202.05376 (2022).
33. S. M. Meenehan, J. D. Cohen, S. Gröblacher, *et al.*, "Silicon optomechanical crystal resonator at millikelvin temperatures," *Phys. Rev. A* **90**, 011803 (2014).
34. A. M. Dibos, M. Raha, C. M. Phenicie, *et al.*, "Atomic source of single photons in the telecom band," *Phys. Rev. Lett.* **120**, 243601 (2018).
35. C. M. Phenicie, P. Stevenson, S. Welinski, *et al.*, "Narrow optical line widths in erbium implanted in TiO<sub>2</sub>," *Nano Lett.* **19**, 8928–8933 (2019).
36. L. Weiss, A. Gritsch, B. Merkel, *et al.*, "Erbium dopants in nanophotonic silicon waveguides," *Optica* **8**, 40–41 (2021).
37. D. F. Walls and G. J. Milburn, *Quantum Optics* (Springer-Verlag, 2008).



## Anomalous Purcell decay of strongly driven inhomogeneous emitters coupled to a cavity: supplement

MICHAEL T. SOLOMON,<sup>1,2,3</sup> MARTIN KOPPENHÖFER,<sup>1</sup> MIKHAIL MAMAEV,<sup>1</sup> CHENG JI,<sup>1,2</sup> GREGORY GRANT,<sup>1,2</sup> IGNAS MASIULIONIS,<sup>1,2</sup> SEAN E. SULLIVAN,<sup>2,3,4</sup> F. JOSEPH HEREMANS,<sup>1,2,3</sup> SUPRATIK GUHA,<sup>1,2,3</sup> DAVID D. AWSCHALOM,<sup>1,2,3,5</sup> AASHISH A. CLERK,<sup>1,2</sup> AND ALAN M. DIBOS<sup>3,6,\*</sup>

<sup>1</sup>Pritzker School of Molecular Engineering, University of Chicago, Chicago, Illinois 60637, USA

<sup>2</sup>Materials Science Division, Argonne National Laboratory, Lemont, Illinois 60439, USA

<sup>3</sup>Center for Molecular Engineering, Argonne National Laboratory, Lemont, Illinois 60439, USA

<sup>4</sup>Current Address: memQ Inc., Chicago, Illinois 60615, USA

<sup>5</sup>Department of Physics, University of Chicago, Chicago, Illinois 60637, USA

<sup>6</sup>Q-NEXT, Argonne National Laboratory, Lemont, Illinois 60439, USA

\* [adibos@anl.gov](mailto:adibos@anl.gov)

---

This supplement published with Optica Publishing Group on 18 June 2024 by The Authors under the terms of the [Creative Commons Attribution 4.0 License](#) in the format provided by the authors and unedited. Further distribution of this work must maintain attribution to the author(s) and the published article's title, journal citation, and DOI.

Supplement DOI: <https://doi.org/10.6084/m9.figshare.25669236>

Parent Article DOI: <https://doi.org/10.1364/OPTICAQ.520843>

# Anomalous Purcell decay of strongly driven inhomogeneous emitters coupled to a cavity – Supplementary Material

MICHAEL T. SOLOMON<sup>1,2,3</sup>, MARTIN KOPPENHÖFER<sup>1</sup>,  
MIKHAIL MAMAEV<sup>1</sup>, CHENG JI<sup>1,2</sup>, GREGORY GRANT<sup>1,2</sup>,  
IGNAS MASIULIONIS<sup>1,2</sup>, SEAN E. SULLIVAN<sup>2,3,4</sup>, F. JOSEPH  
HEREMANS<sup>2,3,1</sup>, SUPRATIK GUHA<sup>1,2,3</sup>, DAVID D.  
AWSCHALOM<sup>1,2,3,5</sup>, AASHISH A. CLERK<sup>1,2</sup>, AND ALAN M.  
DIBOS<sup>6,3,\*</sup>

<sup>1</sup>*Pritzker School of Molecular Engineering, University of Chicago, Chicago, Illinois 60637, USA*

<sup>2</sup>*Materials Science Division, Argonne National Laboratory, Lemont, Illinois 60439, USA*

<sup>3</sup>*Center for Molecular Engineering, Argonne National Laboratory, Lemont, Illinois 60439, USA*

<sup>4</sup>*Current Address: memQ Inc., Chicago, Illinois 60615, USA*

<sup>5</sup>*Department of Physics, University of Chicago, Chicago, Illinois 60637, USA*

<sup>6</sup>*Q-NEXT, Argonne National Laboratory, Lemont, Illinois 60439, USA*

\* *adibos@anl.gov*

## ADDITIONAL EXPERIMENTAL DETAILS

### A. Inverse taper simulations and overall detection efficiency

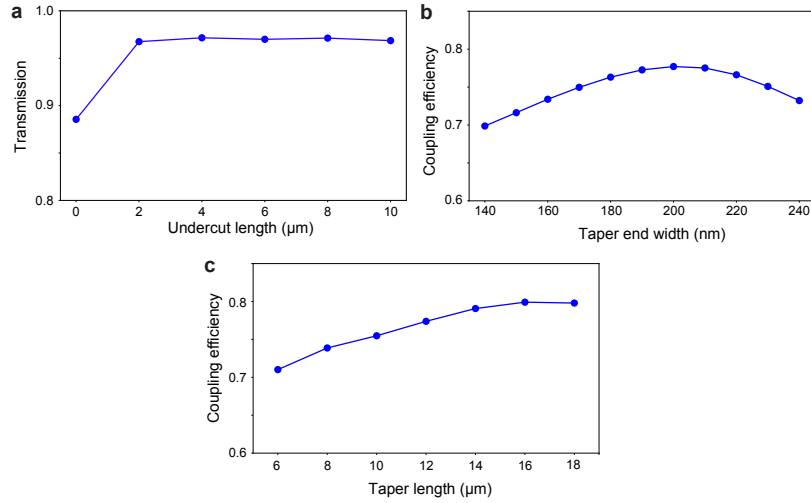


**Fig. S1.** Inverse taper FDTD simulation results. (a) Guided mode transmission as light is routed in a Si waveguide from an undercut region to oxide region. (b) Fiber-to-waveguide coupling efficiency versus waveguide end facet width assuming a fixed taper length of 14  $\mu\text{m}$  and a fixed undercut of 4  $\mu\text{m}$ . (c) Fiber-to-waveguide coupling efficiency versus overall taper length width assuming a fixed end facet width of 200 nm and a fixed undercut of 4  $\mu\text{m}$ .

In order to improve the lensed fiber-to-waveguide coupling efficiency, we implemented a suspended inverse waveguide taper that protrudes off the edge of our sample. This approach is similar to the adiabatic inverse taper designs implemented previously for fully suspended 220 nm thick Si waveguides [1] and 250 nm thick Si waveguides.[2] For our simulations we ignored the presence of our  $\text{TiO}_2$  thin film, because it is only 30 nm thick and the refractive index is smaller than that of Si. In the simulations, we first assumed starting parameters similar to that in previous work: a waveguide end facet width of  $\sim 200$  nm [1] and a taper length of  $\sim 14$   $\mu\text{m}$  [2] for mechanical stability of the tapered region. Then using 3D FDTD (Lumerical), we investigated the minimum extent of the lateral undercut of the buried oxide layer that is needed to sufficiently guide light to the cavity. As shown in Fig. S1a, as long as the initial undercut length is  $\geq 4$   $\mu\text{m}$ , we don't lose much light as the mode transitions into the waveguide region in contact with the buried oxide layer. We then swept around these values to further refine our end facet width (Fig. S1b) and taper length (Fig. S1c) for a fixed undercut length of 4  $\mu\text{m}$ . To do so, we used a TE-polarized Gaussian source with a 1.25  $\mu\text{m}$  waist radius placed 14  $\mu\text{m}$  away from the end of the waveguide to mimic our commercial lensed fiber (OZ Optics) and simulated the transmitted power through a monitor along the waveguide 4  $\mu\text{m}$  after the taper has reached a full width of 650 nm. We can see that for a waveguide end facet width of  $\sim 200$  nm and a taper length of 14  $\mu\text{m}$  we have a maximum one-way coupling efficiency of  $\approx 80\%$  (Fig. S1b). Similarly, in Fig. S1c, we can see that while an increased taper length has slightly higher coupling efficiency, for mechanical reasons we settle on the original taper length of 14  $\mu\text{m}$ .

As discussed in the main text the total detection efficiency for these experiments is 0.023. Beyond the cavity-waveguide coupling efficiency (0.34) and fiber-to-waveguide coupling efficiency (0.65), the additional culprits for the overall system detection efficiency moving (in order) from the lensed fiber to the detector within the collection path are: (1) our circulator, which is designed for use at 1550 nm and has an approximate efficiency of 0.58 at 1520.52 nm, (2) the fiber polarization controller, which has a transmission efficiency of 0.84 due to insertion loss, (3) a fiber-coupled AOM in the collection

channel to protect the detector from latching in the higher incident power cases, which has a transmission of 0.37 at 1520.5 nm due to insertion loss, (4) a fiber-based switch (allows us to alternate between SNSPD counting and photodiode detection for reflection measurements) and other associated fiber-to-fiber coupling losses give a transmission efficiency of 0.73, and (5) the external detection efficiency of our SNSPD is 0.80 at this wavelength. Therefore our total detection efficiency ( $\eta_{total}$ ) is:

$$\eta_{total} = 0.65 \times 0.34 \times 0.58 \times 0.84 \times 0.37 \times 0.73 \times 0.80 = 0.023.$$

## B. Nanofabrication process and cavity characterization

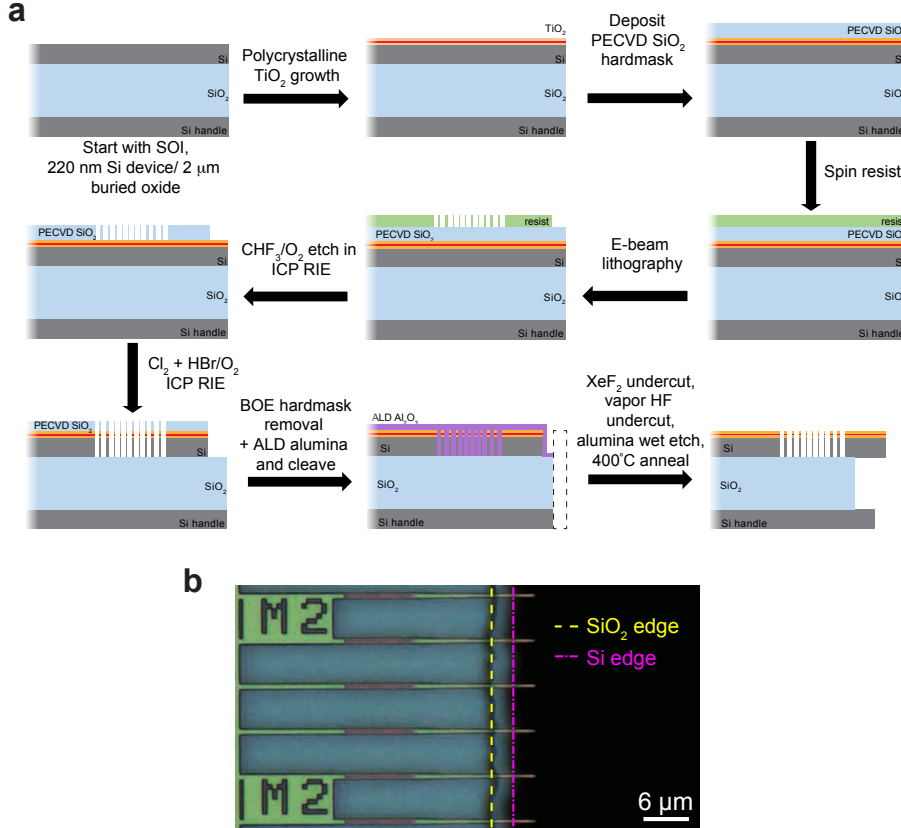


**Fig. S2.** Generating undercut waveguide devices. (a) Full fabrication process flow for undercut waveguide devices. (b) Optical microscope image showing fully suspended devices with the dashed yellow (magenta) lines marking the undercut boundary for the  $\text{SiO}_2$  (Si handle) edges.

The various fabrication steps to generate cavities and suspended inverse tapers along with a optical device image are shown in Fig. S2. All steps in the process flow are performed at the Center for Nanoscale Materials cleanroom at Argonne National Lab. Our  $\text{TiO}_2$  thin films are grown on silicon-on-insulator (SOI) substrates (Soitec) with a lightly boron-doped 220 nm thick Si device layer, 2 μm buried oxide, and a more heavily boron-doped Si handle to reduce charging during subsequent fabrication steps. It is important to note that we deposit a device protection layer consisting of 200 cycles (20 nm) of thermal ALD alumina at a temperature of 175°C because polymeric resist layers do not provide sufficient protection, especially during the vapor HF step. We use this thickness and growth temperature of the alumina layer to mitigate pinholes that would allow the vapor etchants to attack the device layers during the undercut. Immediately after cleaving (Lattice Ax), we isotropically etch the Si handle layer in a  $\text{XeF}_2$  vapor etch tool, which is what gives the sample a scalloped edge (Fig. 1(b)) in the

main text and Fig. S2b). A long delay between the cleaving step and  $\text{XeF}_2$  etch process enables the formation of native oxide on the freshly cleaved Si surface, thereby slowing the otherwise deterministic etch rate of Si with  $\text{XeF}_2$ . After the Si handle undercut step, we then perform vapor HF etching (SPTS uEtch system) to undercut the buried thermal oxide layer. It is the order of these two vapor processes that gives the two-tiered undercut geometry shown in Fig. 1(b) of the main text. We gently strip the alumina ALD layer using Aluminum Etchant Type A (Transene) at 40°C. Finally, to mitigate any potential detrimental defects introduced by the various nanofabrication processes, we anneal the devices in pure  $\text{O}_2$  at 400°C using a rapid thermal annealing system (Annealsys). As discussed in Section A, while our simulations suggest that longer tapers ( $> 14 \mu\text{m}$ ) have a slight improvement in the coupling efficiency, they also become much more fragile during the VHF undercut process because of strain in the suspended  $\text{SiO}_2$  and alumina layers after the Si handle undercut.

In order to compensate for run-to-run etch rate variations, our fabricated devices are designed to have a deliberate elliptical hole size parameter sweep, and so the cavity resonances on each chip range from 1510-1550 nm. Since we are coupling to the Er:rutile  $\text{TiO}_2$  transition at 1520.52 nm, the ideal device resonances are approximately 1530-1532 nm at room temperature to account for the 12 nm resonance blueshift when cooled to 3.5 K. We also know from experience that the cavity Q is limited by scattering loss from fabrication imperfections, so we can use the various visibility parameters in the reflection scan to estimate the waveguide-cavity coupling efficiency ( $\eta = 34\%$ ). Once we know the cavity resonance, we can detune the laser and measure the reflected laser power from the cavity. Comparing this value to the input power provides an estimate of the one-way fiber-to-waveguide coupling efficiency, this critical parameter doesn't affect later comparison with simulations, but it does determine output photon count rate and hence the experimental integration time needed for good enough signal-to-noise to enable lifetime fitting. We choose the highest laser power in our optical experiments ( $\phi = 1.1 \times 10^4 \kappa$ ) to be below the threshold where the Si portion of the cavity heats due to 2-photon absorption (and blueshifts the cavity resonance via gas desorption) [3] when CW laser excitation is incident at 3.5 K.

### C. Cavity-coupled transient spectral hole burning measurements

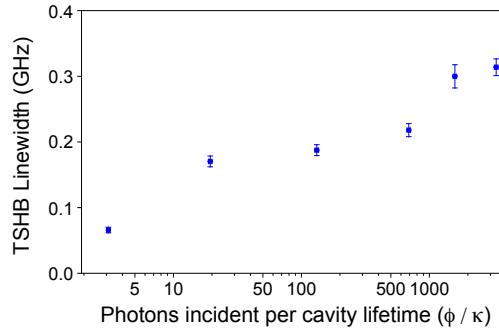


**Fig. S3.** Cavity-coupled transient spectral hole burning (TSHB) measurements as a function of input photon flux at 3.5 K.

We use transient spectral hole burning (TSHB) measurements to get an upper bound on the homogeneous linewidth for the sub-ensemble of ions that couples to the optical cavity.[4] For this measurement we use a similar laser pumping and collection sequence (Fig. 2a of the main text) as for the optical lifetime measurements (Fig. 2c-d of the main text) to probe the emitter linewidths on the relevant pumping timescales. The primary differences for the TSHB measurements are: (1) we sweep the laser sideband frequency via a electro-optic phase modulator (as discussed in prior work [3, 5]), and

(2) we use a reduced number of experimental shots ( $N_{shots}=500$  per carrier-sideband detuning frequency), which results in a shorter overall integration time. We do this because our primary concern is the change in fluorescence intensity as a function of carrier-sideband detuning as opposed to acquiring sufficient signal-to-noise for accurate lifetime fitting, and this allows us to integrate quickly enough to avoid the longer timescale intensity fluctuations discussed in Section E. Also, because we are probing the ions that are coupled to the cavity resonance, we adjust the collected intensity to account for the Lorentzian cavity lineshape ( $\kappa=2.94 \pm 0.05$  GHz). The resultant plot (Fig. S3) shows that the TSHB linewidth (HWHM) versus incident flux seems to saturate near 300 MHz, though we have no intensity contrast at the highest pump fluxes used for the experiments in Figs. 2(c)-(d) of the main text because we are saturating the ions regardless of carrier-sideband detuning. This is supported by the saturation of the integrated intensity presented in Fig. 2(e) of the main text. We assume that at higher pump fluxes that we are likely still in this range, which is narrower than the cavity linewidth and so the ions coupled to the cavity are still in the ‘bad cavity’ limit even for the highest pump powers used in the experiment.

#### D. Bare waveguide ensemble lifetime

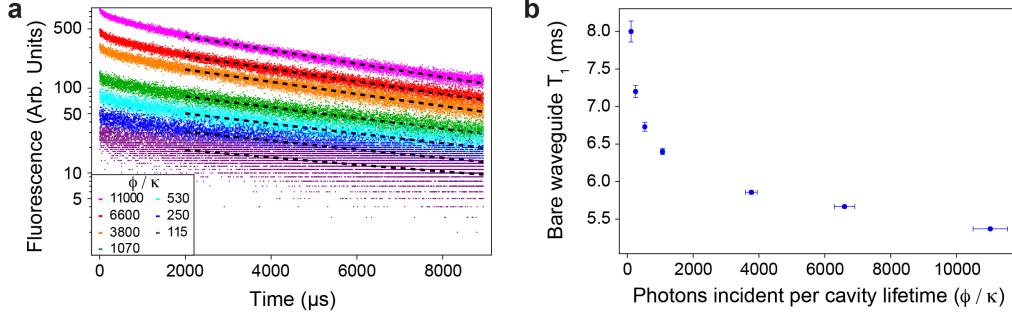


**Fig. S4.** Optical lifetime ( $T_1$ ) estimates from Er ensembles in rutile phase  $\text{TiO}_2$  coupled to bare waveguides. (a) A plot of the bare waveguide measured fluorescence decay curves for most of the incident fluxes shown in Fig. 2(d) of the main text. The dashed black lines are single exponential fits. (b) The extracted single exponential optical lifetime ( $T_1$ ) values for the time traces in (a).

In order to determine a cavity-mediated decay rate enhancement, as shown in Fig. 2(d) of the main text, we need to measure the decay rate ( $\Gamma_0 = 1/T_1$ ) of emitters in our devices without cavity-coupling. We use bare waveguides fabricated on the same chip as the nanocavities, that do not have etched holes but do have the same suspended inverse taper structures. Using the same pulse sequence depicted in Fig. 2(a) of the main text with a resonant pump at  $\lambda = 1520.52$  nm (but with a longer collection time of 8.95 ms and  $N_{shots} = 10^5$  per incident flux), we obtain the fluorescence decay curves shown in Fig. S4a. It is clear that at higher incident powers the fluorescence has a slow exponential tail and a faster decaying component. This may be due to fabrication-induced recombination or other effects, but the origin isn’t currently understood. Without knowing the origin of this effect, we don’t know if these faster sub-ensembles will couple to the cavity mode. For simplicity, we extract a bare emitter lifetime using a single exponential fit to the slower exponential tail. The results of these single exponential fits are shown in Fig. S4. We naively assume a single value of  $\Gamma_0 = 1/T_1$  in Fig. 2(d) of the main text, using the exponential lifetime fit value of  $T_1 = 5.370 \pm 0.013$  ms extracted for the hardest optical drive at  $\phi \sim 11000\kappa$ . This value is in good agreement with  $T_1 = 5.25 \pm 0.03$  ms measured in previous work on Er implanted in rutile phase  $\text{TiO}_2$  [6]. Even for our waveguide devices, this is in reasonable agreement with molecular dynamics simulations of the vacuum decay rate for this transition [7]  $A_{MD} \approx 10$  Hz and  $1/T_1 = A_{MD} n^3$ ,

where  $n$  is the refractive index of the host material. For rutile  $\text{TiO}_2$ ,  $n = 2.45 - 2.70$  depending on dipole orientation [8], resulting in an optical  $T_1 = 5.1 - 6.7$  ms.

### E. PLE and integrated intensity measurements

For the sake of clarity, in Fig. S5 we have replotted the data contained within Fig. 2(c) of the main text into three subpanels and grouped by incident photon flux. Furthermore, we have recolored the various cavity-laser detuning ( $\Delta_C$ ) values to better delineate the trend of each at longer timescales.

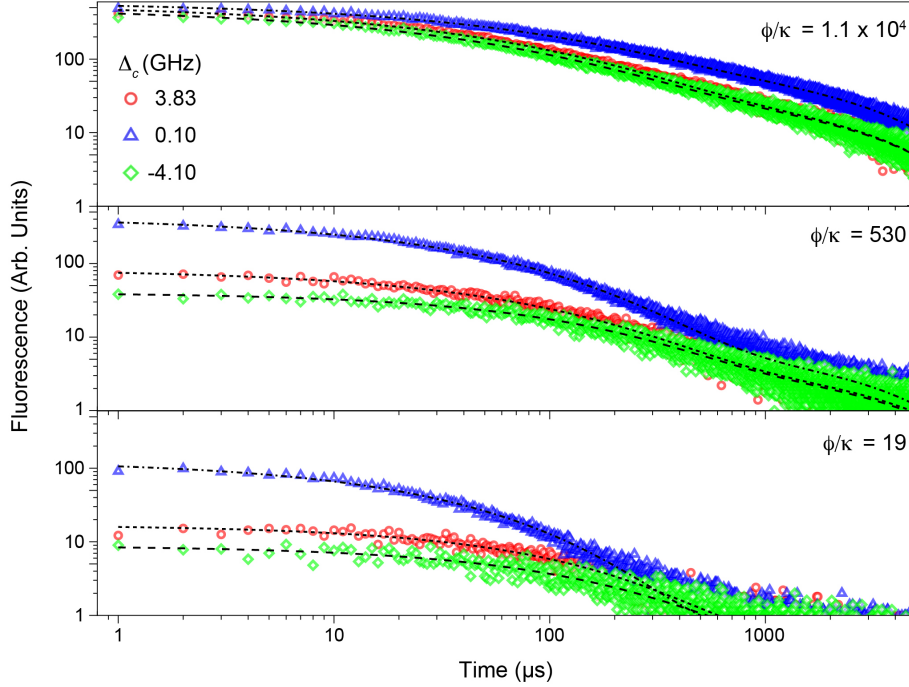


**Fig. S5.** Individual optical decay curves for selected incident photon flux ( $\phi/\kappa$ ) and cavity-laser detuning ( $\Delta_C$ ) values. These curves are the same as in Fig. 2(c) of the main text with an alternate color scheme to better visualize decay for each detuning.

Within our optical setup, we experience periodic intensity fluctuations on the timescale of 15-20 minutes. We suspect that the origin of these intensity fluctuations is because the excitation path of our fiber network is composed entirely of polarization maintaining (PM) components with the exception of 1) the lensed optical fiber, which is machined from a conventional single mode fiber (OZ Optics), and 2) a motorized fiber polarization controller (Phoenix Photonics). The polarization injected into the lensed fiber is first rotated via the polarization controller and set at the beginning of each experiment to match the TE-like polarization of our cavity devices at 3.5 K. During the measurements, likely due to fiber strain induced by thermal gradients within the cryostat when cold (we do not see these effects when warm), there is a modest modification of the polarization within the fiber affecting the injection power into the cavity. More significant is that as photons are routed back through the network for detection, the  $\sim 22$  dB polarization rejection ratio of our PM fiber circulator (Thorlabs) affects the intensity transmitted for detection. These effects are why we perform five full sweeps over the incident power for a given detuning ( $\Delta_c$ ) and then average the resultant lifetime histograms (bin-by-bin). We then fit these averaged histograms to extract the stretched exponential time constants (for the experimental curves within Figs. 2(c)-(d) of the main text) and integrated intensity (Fig. S6). Overall, the time constant fitting is robust to these fluctuations but the detected intensity is not. We are attempting to solve this problem moving forward

with spliced PM lensed fibers.

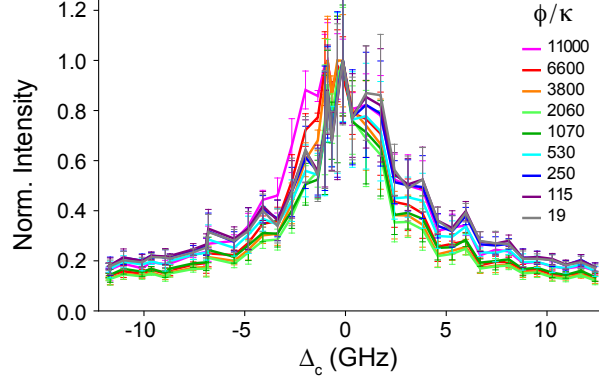


**Fig. S6.** Normalized PLE intensity as a function of cavity detuning ( $\Delta_c$ ) for the various incident photon flux per  $1/\kappa$ . The error values for each data point come from the standard deviation in the integrated PLE intensity from the five measurements per detuning.

#### F. Purcell decay measurements for Er in anatase TiO<sub>2</sub>

On the same growth chip, we also have Er<sup>3+</sup> ions embedded in the anatase phase grains of TiO<sub>2</sub> with a similar brightness and inhomogeneous linewidth to that of rutile grains, as has been seen previously [3]. We can couple optically to these ions in anatase grains using slightly redshifted cavities ( $\lambda \approx 1532.6$  nm) to those presented in the main text. We can perform nearly identical PLE measurements and Purcell-enhanced decay analysis, and an example is shown in Fig. S7, where the cavity  $Q = 6.89 \pm 0.23 \times 10^4$  is nearly identical to, and the cavity-to-waveguide coupling ( $\eta = 0.48$ ) and cavity-to-fiber coupling efficiency (0.67) are slightly better than the rutile TiO<sub>2</sub> case measured in Fig. 1(c) of the main text. The most significant differences between two host phases are that (1) Er in anatase TiO<sub>2</sub> has a shorter natural optical lifetime of  $\sim 1.5$  ms and (2) the extent the lobe separation seems to be less pronounced for the same incident pump power than that of the rutile case. However, the qualitative evolution of the anomalous Purcell slowing with increasing pump flux and the maximum Purcell enhancement extracted from the decay curves are quite similar to the rutile case.

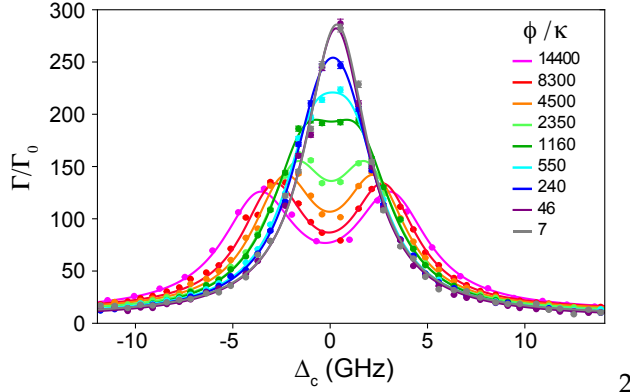


**Fig. S7.** PLE measurements on cavity-coupled Er anatase ensemble at 3.5 K using 2  $\mu$ s resonant laser pulses. The spontaneous decay rate enhancement ( $\Gamma/\Gamma_0$ ) is plotted as a function of the cavity-laser detuning ( $\Delta_c$ ) for increasing incident laser photon flux ( $\phi$ ).

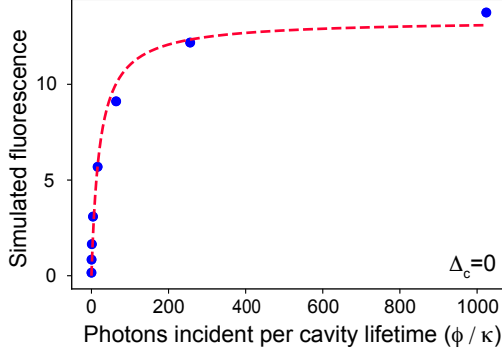


**Fig. S8.** Simulated average PLE intensity a function of incident flux ( $\Delta_c=0$ ). Total fluorescence  $\mathcal{F}$  after subtracting the decay of the initial photon field, defined in Eq. (S2), as a function of the input photon flux  $\phi$ . The dashed fit function represents the PLE function (Eq. (1) of the main text) and is used to determine the critical flux  $\phi_0$  where saturation effects start to become relevant.

## ADDITIONAL SIMULATION DETAILS

### G. Integrated PLE from simulation values

To obtain a reference scale for the input flux  $\phi$  in our simulation, we consider the fluorescence of the spins for a resonant cavity,  $\Delta_c = 0$ . In the experiment, where the photon decay timescale  $1/\kappa$  is much shorter than the timescale on which the ions decay optically through the cavity, the fluorescence can be determined by integrating the number of photons impinging on the detector over the entire photon collection window. In our simulations, these two timescales are less clearly separated. Therefore, we consider a modified definition of the disorder-averaged fluorescence,

$$\overline{F_{\text{sub}}(t)} = \overline{F(t)} - \kappa_c |a(t_{\text{pulse}})|^2 e^{-\kappa(t-t_{\text{pulse}})}, \quad (\text{S1})$$

which subtracts the photons generated by the exponential decay of the initial state of the cavity field. An equivalent of the number of integrated counts (Fig. 2(e) of the main text) can now be obtained by integrating  $\overline{F_{\text{sub}}(t)}$  over the entire photon collection window,

$$\mathcal{F} = \int_{\text{collection window}} dt \overline{F_{\text{sub}}(t)}. \quad (\text{S2})$$

We fit  $\mathcal{F}$ , presented in Fig. S8, to the PLE function given by Eq. (1) of the main text. For this fit function,  $\phi_0 = 1/p_2$  determines the critical photon flux at which saturation effects start to become relevant and serves as a reference scale that allows us to compare our experimental data set from Fig. 2(e) of the main text with our numerical simulations.

### H. Comparison between semiclassical simulation and experiment

We compare the experimental measurements, shown in Fig. 2(d) of the main text, with the semiclassical simulations, shown in Fig. 3(b) of the main text, using two figures of merit. First, we investigate the ratio between the maximum decay rate  $\Gamma$  at a given input flux  $\phi$ ,  $\max_{\Delta_c}(\Gamma|\phi)$ , and its corresponding value at the smallest input flux  $\phi_{\min}$ ,  $\max_{\Delta_c}(\Gamma|\phi_{\min})$  as a function of the rescaled flux  $\phi/\phi_0$ . The corresponding results are shown in Fig. S9a. We find that the semiclassical model roughly agrees with the experimental data for  $\phi/\phi_0 \ll 1$ . Here,  $\phi_0$  is the critical flux above which saturation effects start to become relevant and can be extracted from fits of the integrated fluorescence to the PLE curve Eq. (1) of the main text,  $\phi_0/\kappa = 1/p_2$ , as described in Section G. In the opposite regime  $\phi/\phi_0 \gg 1$ , the semiclassical model deviates from the experimental measurements, likely because the ratio  $\Delta_{\text{inh}}/\kappa$  in the numerical simulations is much smaller than its corresponding value in the experiment.

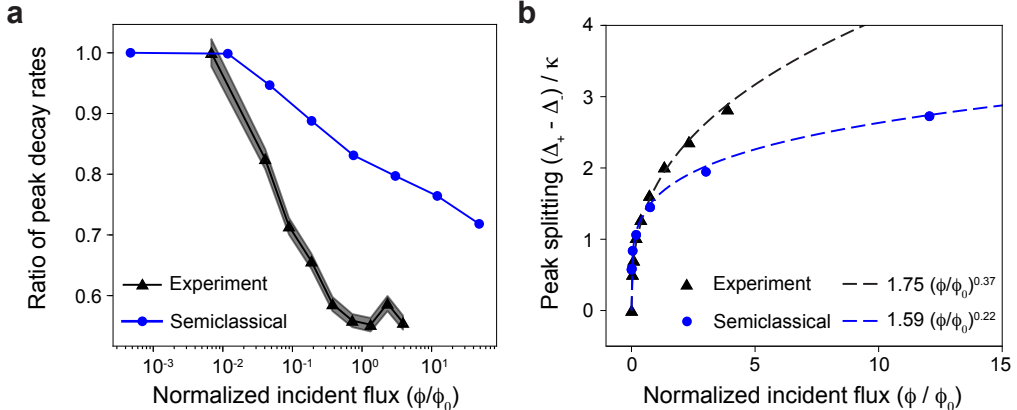


**Fig. S9.** Comparison between the experimental measurements and the results of the semiclassical simulations. (a) Maximum decay rate ratio as a function of the incident flux  $\phi$  relative to the corresponding value for the smallest incident flux,  $\max_{\Gamma}(\Gamma)/\max_{\Gamma}(\Gamma|_{\phi_{\min}})$ , as a function of the photon flux ( $\phi$ ), normalized to the critical photon flux ( $\phi_0$ ) where saturation effects start to occur. The gray shaded areas indicate the standard deviation of the experimental data. (b) Separation of the two maxima ( $\Delta_{\pm}$ ) in the fluorescence decay rate  $\Gamma$  as a function of  $\phi/\phi_0$ .

Second, we compare the dependence of the separation  $\Delta_+ - \Delta_-$  between the two peaks of the decay rate  $\Gamma$  as a function of  $\phi/\phi_0$ . The peak positions  $\Delta_{\pm}$  have been extracted from Lorentzian fits of the data as described in the main text. For this figure of merit, we find that both data sets agree very well in the regime  $\phi/\phi_0 \lesssim 1$ , where the range of detuning for which spins are highly depolarized to  $s_z^j \approx 0$  is much smaller than the finite extent  $\Delta_{\text{inh}}$  of the inhomogeneous frequency distribution. The inhomogeneous broadening  $\Delta_{\text{inh}}$  defines an upper bound on the maximum possible splitting  $\Delta_+ - \Delta_-$ , since it controls the spectral extent of the ion ensemble. In the semiclassical simulations, we use a smaller value of  $\Delta_{\text{inh}}$  than in the experiments, such that finite size effects of the ion ensemble will manifest themselves more pronouncedly with increasing input power.

### I. Frequency-resolved decay dynamics

The semiclassical model introduced in the main text allows us to study the decay dynamics of spins as a function of their detuning  $\delta_j$ . To this end, we employ the following binning procedure. For each disorder realization, we assign each spin to a frequency bin of width  $0.167\kappa$  based on their random detuning  $\delta_j$ . Averaging over many realizations, we can then compute the average time-dependent spin excitation  $1 + s_z^j$  in each frequency-resolved bin. We present results for the case  $\Delta_c = 0$  in Fig. S10.

The distribution of the mean spin excitation of the initial state at time  $t_{\text{pulse}}$  is given by the red stars in Fig. S10 and matches well the theory expression:

$$s_{z,\text{ss}}^j = -1 + \frac{8|\bar{a}_{\text{ss}}|^2 \bar{g}^2}{8|\bar{a}_{\text{ss}}|^2 \bar{g}^2 + \gamma^2 + 4\delta_j^2}, \quad (\text{S3})$$

which is Eq. (10) of the main text with  $g_j$  replaced by  $\bar{g}$ . The light red shaded region on the initial state curve in Fig. S10 represents the standard deviation of the mean spin excitation in each bin. Fig. S10 shows that, as the spins fluoresce, the mean spin excitation in each bin decreases. Surprisingly, we find that for sufficient drive strengths, spins that are resonant with the cavity ( $\delta_j \approx \Delta_c = 0$ ) decay far slower than spins with a large detuning.

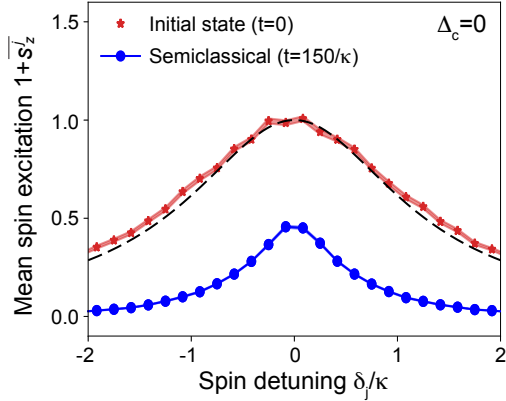


**Fig. S10.** Mean spin excitation  $1 + \bar{s}_z^j$  as a function of spin detuning  $\delta_j$  for the initial state immediately after the laser excitation pulse (red stars) and at  $t = 150/\kappa$  after the pulse (blue dots). The dashed black curve is the theory expression for the mean spin excitation, Eq. (10) of the main text with  $g_j$  replaced by  $\bar{g}$ . The cavity is resonant with the drive laser,  $\Delta_c = 0$ .

### J. Three spin toy model

Here we provide details on the simple three-spin toy model presented in the main text. This model considers semi-classical evolution of three spins labeled  $\nu = \{0, L, R\}$  with respective spin operators  $s_\alpha^\nu$  for  $\alpha \in \{+, -, z\}$ , respective detunings  $\delta_\nu = \{0, -\delta_S, +\delta_S\}$  for a fixed  $\delta_S$ , and respective spin sizes  $N^\nu$  (represented schematically in Fig. S12a). The equations of motion are:

$$\begin{aligned} \frac{d}{dt}a &= -\left(i\Delta_c + \frac{\kappa}{2}\right)a - ig\left(s_-^0 + s_-^L + s_-^R\right), \\ \frac{d}{dt}s_-^\nu &= -\left(i\delta_\nu + \frac{\gamma}{2}\right)s_-^\nu + igas_z^\nu, \\ \frac{d}{dt}s_z^\nu &= 2ig(a^*s_-^\nu - as_+^\nu) - \gamma(N^\nu + s_z^\nu). \end{aligned} \quad (\text{S4})$$

We assume a symmetric ensemble with  $N^L = N^R$ . The initial conditions are:

$$\begin{aligned} a(0) &= \bar{a}_{ss} = \frac{i\sqrt{\kappa_c}\beta_{in}}{\Delta_c - i\frac{\kappa}{2}}, \\ s_-^\nu(0) &= -\frac{2(2\delta_\nu + i\gamma)g\bar{a}_{ss}N^\nu}{8g^2|\bar{a}_{ss}|^2 + \gamma^2 + 4\delta_\nu^2}, \\ s_z^\nu(0) &= -N^\nu + \frac{8g^2|\bar{a}_{ss}|^2N^\nu}{8g^2|\bar{a}_{ss}|^2 + \gamma^2 + 4\delta_\nu^2}. \end{aligned} \quad (\text{S5})$$

Contributions from the spins to the steady-state cavity field in the denominator for  $\bar{a}_{ss}$  are neglected for simplicity, as they do not qualitatively change the physics of the toy model.

In Fig. S11a the initial conditions for the spin observables are shown as a function of initial cavity field  $|\bar{a}_{ss}|$ . For sufficiently strong driving  $g|\bar{a}_{ss}| \gg \gamma$  the resonant spin is nearly depolarized with  $s_-^0, s_z^0 \approx 0$ . The off-resonant spin excitation fraction  $s_z^{L/R}$  uniformly increases with  $|\bar{a}_{ss}|$ , and approaches a fully depolarized state  $s_z^{L/R} = 0$  as  $|\bar{a}_{ss}| \rightarrow \infty$ . However, the spin coherence  $s_-^{L/R}$  is non-monotonic, and exhibits a maximum in magnitude at

$$\bar{a}_{ss} = \frac{\sqrt{\gamma^2 + 4\delta_S^2}}{2\sqrt{2}g} = \frac{\delta_S}{\sqrt{2}g} + \mathcal{O}\left(\frac{\gamma^2}{\delta_S^2}\right). \quad (\text{S6})$$

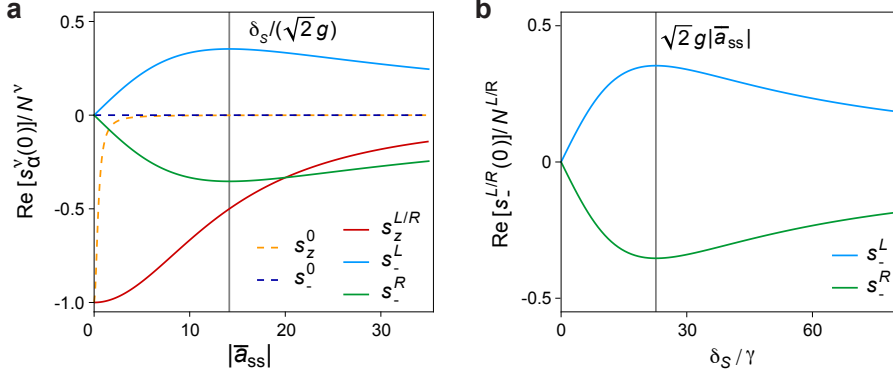


**Fig. S11.** (a) Initial spin observables for the three-spin toy model from Eq. (S5) as a function of cavity field magnitude  $|\bar{a}_{ss}|$ , with a fixed off-resonant spin detuning  $\delta_S/\gamma = 16$  and spin-cavity coupling  $g/\gamma = 0.8$ . Dashed and solid lines correspond to resonant and off-resonant spins respectively. The cavity field  $\bar{a}_{ss}$  is taken real without loss of generality, and only the real part of the spin coherences  $s_-^v$  is plotted; the imaginary part is negligible in comparison for  $g|\bar{a}_{ss}| \gg \gamma$ . The vertical gray line shows a cavity field at which off-resonant spins exhibit maximal coherence, which is equal-and-opposite for the left and right spins due to their opposite detuning sign. (b) Off-resonant spin coherence (again taking the real part) for fixed cavity field  $\bar{a}_{ss} = 20$  and spin-cavity coupling  $g/\gamma = 0.8$ , as a function of spin detuning  $\delta_S/\gamma$ . The same maximum as panel (a) is shown via the vertical line.

At a fixed light field  $\bar{a}_{ss}$ , there is an optimal spin detuning  $\delta_S$  at which the system has maximum transverse polarization. Inverting this equation, we get

$$\delta_S = \frac{1}{2} \sqrt{8g^2|\bar{a}_{ss}|^2 - \gamma^2} = \sqrt{2}g|\bar{a}_{ss}| + \mathcal{O}\left(\frac{\gamma^2}{g^2|\bar{a}_{ss}|^2}\right). \quad (\text{S7})$$

This gives a reasonable detuning that captures the effect of the most relevant off-resonant spins in the full inhomogeneously broadened ensemble. Fig. S11b shows the off-resonant spin coherences as a function of spin detuning  $\delta_S$ , showing that this maximum persists. At this detuning, the initial conditions of the off-resonant spins are:

$$\begin{aligned} s_-^L(0) &= +\frac{N^L}{2\sqrt{2}} \frac{|\bar{a}_{ss}|}{\bar{a}_{ss}^*} + \mathcal{O}\left(\frac{\gamma}{g|\bar{a}_{ss}|}\right), \\ s_-^R(0) &= -\frac{N^R}{2\sqrt{2}} \frac{|\bar{a}_{ss}|}{\bar{a}_{ss}^*} + \mathcal{O}\left(\frac{\gamma}{g|\bar{a}_{ss}|}\right), \\ s_z^{L/R}(0) &= -\frac{N^{L/R}}{2} + \mathcal{O}\left(\frac{\gamma^2}{g^2|\bar{a}_{ss}|^2}\right). \end{aligned} \quad (\text{S8})$$

These initial values scale macroscopically with spin size  $N^{L/R}$  provided the initial cavity field satisfies  $g|\bar{a}_{ss}| \gg \gamma$ .

Note that in the main text we take the sizes of the off-resonant spins to be much larger than the resonant ones,  $N^L = N^R \gg N^0$ . This is done because as shown in Fig. S11b, the spin coherence exhibits a maximum at a characteristic intermediate spin detuning  $\delta_S$ , but falls off very slowly as detuning is further increased, scaling as  $\sim 1/\delta_S$ . Hence regardless of the characteristic detuning magnitude, a large selection of off-resonant spins from the full ensemble will participate in the Purcell-enhanced relaxation dynamics. For an ensemble with strong inhomogeneous broadening, this relevant frequency range is much larger than the range containing resonant spins  $N^0$  which are fully depolarized (and thus require  $g|\bar{a}_{ss}| \gg \gamma$ ).

We also take  $N^0, N^L, N^R$  to be independent of cavity field strength  $|\bar{a}_{ss}|$ . This is done for simplicity, as the more relevant factor is the ratio of the frequency ranges containing the resonant- and off-resonant spins, both of which scale with  $|\bar{a}_{ss}|$ . A more

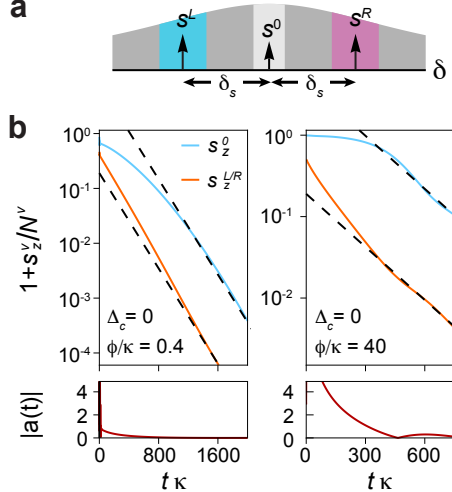


**Fig. S12.** Relaxation dynamics for a toy three-spin model. (a) Schematic of the model, using one resonant spin  $s^0$  and two off-resonant spins  $s^{L/R}$  with detunings  $\pm\delta_s$  with  $\delta_s \approx \sqrt{2g|\bar{a}_{ss}|}$ . (b) Decay dynamics of the spins and cavity for different initial pulse  $\phi/\kappa = 0.4, 40$  for fixed  $\gamma = 0.005/\kappa, g = 0.004\kappa, N^0 = 2,000, N^{L/R} = 40,000$ . Black dashed lines are intrinsic decay  $\sim e^{-\gamma t}$ . For a strong drive pulse, there is no appreciable short-time decay of  $s_z^0$ .

careful analysis can be performed which scales the sizes of the spins based on how their coherence varies across frequency space, but we leave such investigation to future work.

Aside from the simulation shown in the main text, here we also show details on the relaxation dynamics of the three-spin model. Fig. S12b plots the decay of both the spin excitations and the cavity field at cavity resonance  $\Delta_c = 0$ . While the off-resonant spins undergo Purcell decay as expected, for stronger initial laser power (larger  $\phi$ ) we find a striking enhanced survival of the resonant spin, which remains nearly depolarized over a long timescale before resuming intrinsic decay  $\sim e^{-\gamma t}$ . This slow initial relaxation and lack of Purcell decay matches the behaviour seen in the semiclassical disorder-averaged simulations. As described in the main text, the resonant spin cannot decay into the cavity on its own because it lacks coherence  $s_z^0 \approx 0$ . Relaxation of the resonant spin due to spontaneous decay is further impeded by a second effect involving the non-resonant spins  $s^L, s^R$ . As these spins Purcell decay and hence pump excitations into the cavity, this effective pumping also generates a transient cavity field, shown in the plots at the bottom of Fig. S12b. This transient field can directly drive the resonant spin  $s_z^0$ , which keeps it excited provided the effective driving rate  $\sim g|a|$  is stronger than the loss rate  $\gamma$ . As seen in the figure, the expected intrinsic decay of the resonant spins resumes as soon as the off-resonant spins finish their Purcell-enhanced decay and the cavity field depletes.

## REFERENCES

1. S. M. Meenehan, J. D. Cohen, S. Gröblacher, *et al.*, “Silicon optomechanical crystal resonator at millikelvin temperatures,” Phys. Rev. A **90**, 011803 (2014).
2. A. M. Dibos, M. Raha, C. M. Phenicie, and J. D. Thompson, “Atomic source of single photons in the telecom band,” Phys. Rev. Lett. **120**, 243601 (2018).
3. A. M. Dibos, M. T. Solomon, S. E. Sullivan, *et al.*, “Purcell Enhancement of Erbium Ions in TiO<sub>2</sub> on silicon nanocavities,” Nano Lett. **22**, 6530–6536 (2022).
4. W. E. Moerner, ed., *Persistent Spectral Hole-Burning: Science and Applications*, vol. 44 of *Topics in Current Physics* (Springer Berlin Heidelberg, Berlin, Heidelberg, 1988).
5. L. Weiss, A. Gritsch, B. Merkel, and A. Reiserer, “Erbium dopants in nanophotonic

- silicon waveguides,” Optica **8**, 40–41 (2021).
- 6. C. M. Phenicie, P. Stevenson, S. Welinski, *et al.*, “Narrow Optical Line Widths in Erbium Implanted in TiO<sub>2</sub>,” Nano Lett. **19**, 8928–8933 (2019).
  - 7. C. M. Dodson and R. Zia, “Magnetic dipole and electric quadrupole transitions in the trivalent lanthanide series: Calculated emission rates and oscillator strengths,” Phys. Rev. B **86**, 125102 (2012).
  - 8. J. Rams, A. Tejeda, and J. M. Cabrera, “Refractive indices of rutile as a function of temperature and wavelength,” J. Appl. Phys. **82**, 994–997 (1997).